Russian Chemical Reviews **82** (2) 131 – 149 (2013) © 2013 Russian Academy of Sciences and Turpion Ltd

DOI 10.1070/RC2013v082n02ABEH004331

Coatings based on calcium phosphates for metallic medical implants

V M Ievlev

Contents

I.	Introduction	131
II.	Calcium phosphates for bioactive coatings	132
III.	Deposition of calcium phosphate coatings	137
IV.	Conclusion	147

Abstract. The calcium phosphate coatings for metallic medical implants that are used to replace the bone tissues synthesized by various methods are considered in the structural and morphological aspects. The advantages and shortcomings and the prospects of application of the methods of deposition of such coatings on metal substrates are discussed. The bibliography includes 132 references.

I. Introduction

The requirements imposed on the materials for medical implants used to replace the bone tissues subjected to large mechanical loads are met only by metal and/or metal alloys. They have high strength and long service life, relatively low elastic moduli and plasticity at the body temperature. Considering the chemical (corrosion resistance, lack of toxicity) and biological † compatibility, the range of applicable implant materials is still restricted to commercially available pure titanium and some titanium alloys (for example, Ti6Al4V, Ti6Al7Nb).

Titanium implants have relatively low density, high strength and good processability. The surface of such implants exhibits bioactivity, which can be mediated through thin natural titanium oxide layers.[2] In the case of finely dispersed grain structure of the metal, which can be achieved by intense plastic deformation, the bioactivity increases:[3] fibroblast colonization of the surface of nanostructured titanium increases more than 1.5-fold as compared with colonization of the initial sample. Doping that increases the mechanical strength of titanium is also favourable for biocompatibility. This was observed for the Ti6Al7Nb alloy with a lower electronic conductivity of the passive oxide layer compared with that of titanium.[4] However, the corrosion stability of titanium implants is higher than that of alloys. Therefore, strengthening of titanium implants with simultaneous increase in the bioactivity of its surface by creating a submicrocrystalline or nanocrystalline structure,[5] which is in line with the tendency toward eliminating the doping components from the implant, appears justified.

From the results of numerous investigations, one can conclude that the properties and functional activity of the surface of a metallic implant can be controlled by forming relief with different degrees of dispersion,[6] oxidation (as is the case for biomimetic coating deposition [2]), formation of a nanoporous oxide [7] or ion-implantation.[8]

Application of synthetic calcium phosphate (CP) coatings is the most effective way of surface modification, which provides osseointegration of metallic implants with bone tissues. Calcium phosphate is the principal mineral component of the bone tissue, and the presence of several calcium phosphate compounds in the coating provides the possibility to control its biochemical activity by changing the phase composition:[9] the rate of resorption of the coating material must correspond to the rate of tissue restoration.

An important requirement imposed on this type of coating is high adhesion and cohesion strength. The attainment of the required cohesion strength is often complicated by the necessity to have a large specific surface area (open porosity) and specific morphology of the coating growth front in some inexpensive coating techniques.

The known monographs,[10, 11] which integrate the results of studying CP and developing CP-based ceramics for medicine,[12, 13] contain sections reflecting, to different extents, the state-of-the-art of research into the synthesis of coatings by the date preceding their publication. The most comprehensive review dealing with the synthesis of coatings was reported by Narayaman *et al.*[14] There are reviews on particular methods (*e.g.*, biomimetic method,[15] plasma spray deposition [16]) and thesis works (*e.g.*, on ion-implantation,[8] high-frequency magnetron sputtering [17]);

V M Ievlev Voronezh State University, Universitetskaya pl. 1, 394006 Voronezh, Russian Federation. Tel. (7-473) 220 87 35, e-mail: rnileme@mail.ru

Received 16 May 2012
Uspekhi Khimii **82** (2) 131 – 149 (2013); translated by Z P Svitanko

† By the definition of the European Society for Materials (1986), this is the ability of the implant to be involved in the adequate set of reactions on its specific application.[1]

The pulsed laser evaporation and magnetron sputtering techniques were compared.[18] However, data on the substructure of apatites and apatite-based coatings are either not considered in the mentioned reviews or restricted to only morphological characteristics. The present review is focused on the substructural features of the coatings, first of all, of hydroxyapatite (HAP), which is the principal and most studied phase of ceramics and coatings.

II. Calcium phosphates for bioactive coatings

The key crystal structure parameters of calcium orthophosphates that are used to manufacture biologically active coatings are summarized in Table 1. The thermodynamically stable and well-organized crystal structure of HAP[19] not only provides the bone tissue with living resource but also ensures its non-plasticity caused by poor translational symmetry of the crystal lattice: the minimum full translation vectors correspond to the basis vectors of the crystal lattice, which are rather long (see Table 1). This lowers the probability of formation of deformation-induced perfect dislocations, because the energy of their origin (proportional to the squared length of the Burgers vector) is rather great. This accounts for high shear strength[20] and hardness[21] of crystals and nanocrystalline coatings.[22] The specific atomic structure should affect the possible dislocation structure of grain boundaries in the polycrystalline HAP because the above-noted peculiarity of the translational symmetry imposes restrictions on the model of grain boundary structure which is based on the views on the coincidence site lattice and grain boundary dislocations.[23]

Only two CPs, namely hydroxyapatite and β-calcium phosphate, are widely used to produce bioresorbable ceramics[12] and coatings. Hydroxyapatite-based ceramics tend to have low rates of resorption, which can be increased by adding β-calcium phosphate. As a way of modification of ceramic properties, various uses of ion-substituted apatites are considered, in particular, silicon-substituted (Si-HAP) and carbonate-substituted (CHA) apatites, fluoroapatite (FA), *etc*. The ionic substitution influences some properties such as the solubility and dispersivity of the grain structure as well as the cell growth and collagen synthesis.[24]

Most of compounds included in Table 1, in particular, β-calcium phosphate, can be formed as intermediates of HAP synthesis or as HAP precursors (Fig. 1) depending on the method. For example, monetite, which is formed on a titanium cathode during electrochemical deposition, is completely converted to HAP when the sample is immersed into a solution of NaOH; ion beam sputtering of an HAP target gives a coating of amorphous calcium phosphate, which crystallizes to give HAP upon the subsequent annealing; high-frequency magnetron sputtering of a calcium phosphate target is accompanied by the synthesis of nanocrystalline HAP coating.

1. Structure

The term 'structure' is used in a broad sense ranging from the atomic structure to the surface morphology, which does not always reflect even the grain structure and, the more so, the intragrain substructure. Note that in the substructural aspect, characteristics such as the phase composition, nanocrystal porosity[19,25] and the morphology of HAP nanopowders prepared by different solution methods[26,27] and the morphological changes that accompany ion substitution[28] have been studied most comprehensively by electron diffraction and transmission electron microscopy (TEM). This may be attributed to the simplicity of sample preparation for TEM and to small thickness of particles suitable for high-resolution TEM (HRTEM).[25] One of the first studies of the substructure of 2 – 10 μm-thick HAP crystals was done by high-voltage TEM (2000 keV).[29] In the crystals oriented by the $(01\bar{1}0)$ plane, linear contrast was identified, which was interpreted as dislocations and dislocation loops in the HAP lattice. However, no attempts were made to determine the Burgers vectors in order to elucidate the nature of the defects.

Porter *et al*.[30] studied the influence of ion substitution on crystal lattice parameters of silicon-substituted HAP by X-ray diffraction and obtained TEM images of the defective HAP and Si-HAP crystals. In the submicrometre-size crystals with the $(2\bar{1}\bar{1}0)$ plane arranged perpendicular to the electron beam, in the reflections $\vec{g}_{0001}$, linear defects were identified, which were interpreted as dislocations with the Burgers vectors $\vec{b} = \langle 0001 \rangle$ or $1/3\,\langle \bar{2}113 \rangle$ and $\vec{b} = 1/3\,\langle 11\bar{2}0 \rangle$ or $1/3\,\langle 1\bar{2}10 \rangle$. In both cases, the study revealed extended well-faceted boundaries arranged almost perpendicular to the axis [0001] of the crystal lattice (this correlates with the shape anisotropy of the HAP powder nanoparticles[28] and with the HRTEM data[31]) and triple junctions of the isotropic grains and subgrains. In the subgrain boundaries, single dislocations counterbalancing the very low misorientation of the corresponding planes were identified. The difference between the grain boundary structures of Si-HAP and HAP was also established; an increase in the silicon content increased the density of grain triple junctions. This is expected to be beneficial for the biological activity.

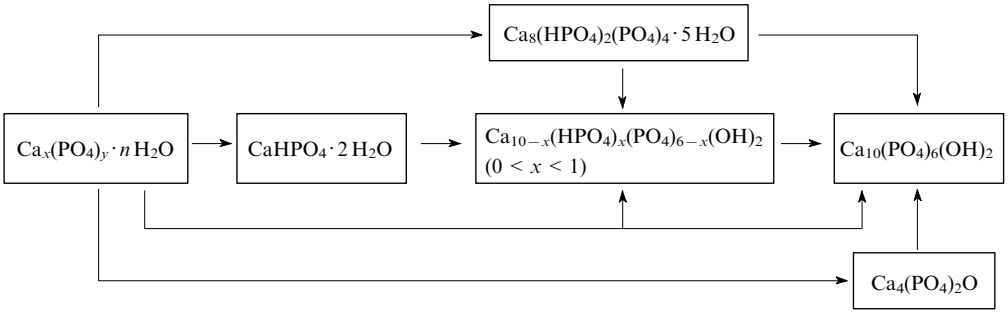


Figure 1. Possible transformations of amorphous calcium phosphate in HAP.

Table 1. Structural characteristics of calcium orthophosphates used for the preparation of coatings (according to the database of the 'International Centre for Diffraction Data', http://www.icdd.com).

Name	Composition	Structural characteristics								Ca : P molar ratio
		crystal system	sp. gr.	a /Å	b /Å	c /Å	α /deg	β /deg	γ /deg	
Calcium dihydrogen phosphate	$Ca(H_2PO_4)_2 \cdot H_2O$	triclinic	$P\bar{1}$	5.6261(5)	11.889(2)	6.4731(8)	98.633(6)	118.262(6)	83.344(6)	0.5
Anhydrous calcium phosphate	$Ca(H_2PO_4)_2$	"	$P\bar{1}$	7.5577(5)	8.2531(6)	5.5504(3)	109.87(1)	93.68(1)	109.15(1)	0.5
Calcium hydrogen phosphate (brushite)	$CaHPO_4 \cdot 2\,H_2O$	monoclinic	Cc	6.227	15.180	5.860	–	116.03(3)	–	1.0
Anhydrous calcium hydrogen phosphate (monetite)	$CaHPO_4$	triclinic	$P\bar{1}$	6.916(2)	6.619(2)	6.946(3)	96.18(3)	103.82(3)	88.34(3)	1.0
Octacalcium dihydrophosphate (tetraphosphate) pentahydrate (octacalcium phosphate)	$Ca_8(HPO_4)_2(PO_4)_4 \cdot 5\,H_2O$	"	P	19.692(4)	9.523(2)	6.835(2)	90.15(2)	92.54(2)	108.65(1)	1.33
α-Calcium phosphate	α-$\hat{o}_3(_4)_2$	monoclinic	$P2_1/a$	12.887(2)	27.280(4)	15.219(2)	–	126.20(1)	–	1.5
β-Calcium phosphate	β-$Ca_3(PO_4)_2$	rhombohedral	$R3c$	10.4264(2)	10.4264(2)	37.376(2)	–	–	120	1.5
Hydroxyapatite [a]	$Ca_{10}(PO_4)_6(OH)_2$	hexagonal	$P6_3/m$	9.41898(19)	9.1898(19)	6.8119(17)	–	–	–	1.67
Calcium-depleted hydroxyapatite	$Ca_{10-x}(HPO_4)_x(PO_4)_{6-x}(OH)_2$ $(0 < x < 1)$									1.5 – 1.67
Calcium pyrophosphate	$Ca_4(PO_4)_2O$	monoclinic	$P2_1$	9.473	11.986(4)	7.023	–	90.0	–	2.0
Amorphous calcium phosphate	$Ca_x(PO_4)_y \cdot n\,H_2O$									1.2 – 2.5

[a] The structure of HAP is analogous to the structure of oxyapatite $C_{10}(PO_4)_6O$ with slight deviation of the unit cell parameter c.

The compact submicrocrystalline ceramics of fluorine-substituted HAP was studied by TEM.[32] For the preparation of dense ceramics, fluorohydroxyapatite (FHA) powders with 10% of the hydroxy groups being replaced by fluoride anions were prepared. Calcium nitrate and ammonium hydrogen phosphate and fluoride were used as the starting compounds. The reactions

$$10\,Ca(NO_3)_2 + 6\,(NH_4)_2HPO_4 + 0.2\,NH_4F + 7.8\,NH_4OH \longrightarrow$$

$$\longrightarrow Ca_{10}(PO_4)_6(OH)_{1.8}F_{0.2} + 20\,NH_4NO_3 + 6\,H_2O$$

carried out at pH > 9 gave a white-synthesized precipitate, which was filtered off and dried to form a gel. After further drying and grinding to form a powder to a < 100 μm particle size, pressing in steel cylindrical press moulds ~ 20 mm in diameter under a 300 MPa pressure was performed. The semitransparent cylindrical pellets thus produced were sintered in air in a muffle furnace at 1050 °C for 1 h. For HRTEM study of the ceramics, cross-section samples were prepared.

Analysis of X-ray diffraction patterns of the samples demonstrated that they were single phases. Figure 2 *a* shows the TEM images of the grain structure of a thinned ceramic sample having a compact submicrocrystal substructure with a grain size of 100 – 300 nm. The grain boundaries and triple junctions have no nanopores or amorphous phase. The largely linear character of grain boundary traces attests to their equilibrium position.

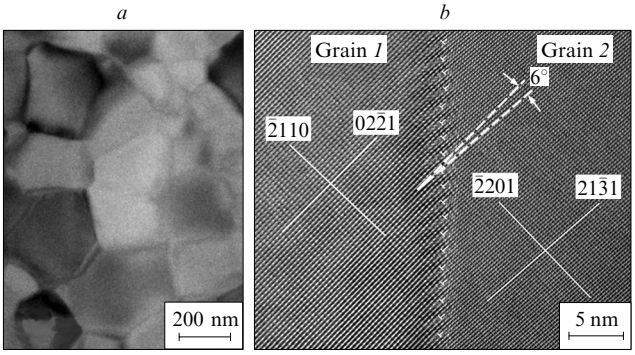


Figure 2. TEM images of the thinned sample of FHA ceramics (*a*) and an area containing grain boundary (*b*).[32]

An example of the dislocation substructure of the high-angle boundary in the FHA ceramics is presented in Fig. 2 *b*. Here within grain *1*, planes (02$\bar{2}$1) and ($\bar{2}$110) are resolved and within grain *2*, planes (21$\bar{3}$1) and ($\bar{2}$201) are resolved. The boundary is nearly perpendicular to the image plane. The regular series of dislocations with 1.6 nm period along the boundary counterbalances the size misfit

$$\frac{d_{02\bar{2}1} - d_{21\bar{3}1}}{d_{02\bar{2}1}} \approx 0.2$$

and misorientation (6°) in the matching of planes (02$\bar{2}$1) and (21$\bar{3}$1). The period of the dislocation series corresponds to the calculated value taking into account the deviation of the boundary plane trace from the perpendicular to the planes being matched.

The matching of planes with different indices formally corresponds to the common type of internal interfaces, because the necessity to counterbalance the size misfit appears, first of all, at phase interfaces. As applied to grain boundaries, the model of plane matching upon crossing the boundary was first proposed by Pumphrey.[33] This model accounted for the periodic substructure of common type high-angle grain boundaries detected by TEM with amplitude contrast in polycrystalline aluminium[34] and some other materials,[34, 35] in particular, rutile films.[35] The cited model[33] considers matching of the most close-packed low-index planes at the grain boundary. Kosevich *et al.*[36] used the high-angle boundary in multiorientation epitaxial aluminium films to demonstrate consistency of the plane matching model and the model based on the coincidence site lattice concept and grain boundary dislocations. The Burgers vectors of grain boundary dislocations correspond to the basis of the lattice displacements,[23] which preserve the coincidence lattice.[23] Analysis showed that extension of this concept to grain boundaries in hydroxyapatite has no sense due to poor translational symmetry of its crystal lattice: the basis vectors of grain boundary dislocations for all special boundaries correspond to full translation vectors.

Evidently, systematic observations of the dislocation substructure of high-angle grain boundaries of HAP in various items (bulk ceramics, coatings) would contribute to the understanding of the nature of microplasticity manifested during nanoindentation[37] and would confirm the necessity to take into account the real substructure for considering the kinetics of biochemical processes.

The HAP/amorphous phase interface, more precisely, the atomic structure of the faceting surface of the crystalline phase of HAP in the amorphous matrix was studied by HRTEM.[31] It was shown that the crystal surface is parallel to surface (10$\bar{1}$0). This attests to its low energy and is consistent with the equilibtium shape of the HAP crystal whose prismatic faces are designated as {10$\bar{1}$0}. It follows from TEM images that the boundary faceted by this plane crosses the OH sites, the calcium atoms and the PO_4 tetrahedra.

Calcium-deficient hydroxyapatite (CDHA) can decompose to stoichiometric HAP and β-calcium phosphate when annealed up to 850 °C. Since this HAP is of great interest for biomedical applications (it participates in the bone formation processes and is the precursor of the HAP + β-calcium phosphate composite having higher biological activity than single-phase HAP), studies of its decomposition and structural transformations are in progress. Decomposition of CDHA is accompanied by structural changes, particularly, a metastable phase with a high Ca : P ratio is formed in the temperature range of 700 – 800 °C, which is coherently matched to the (10$\bar{1}$0) plane of elongated HAP particles (2 – 5 μm along the *c* axis and 0.1 μm across this axis).[38] The periodicity found in the ~ 5 nm-thick metastable phase was 1.43 nm (with $d_{10\bar{1}0} = 0.816$ nm). It was assumed that the metastable phase is formed upon accumulation of calcium ions, and in the calcium-depleted region, β-calcium phosphate is formed. Using selected area electron diffraction, the unit cell parameters of the metastable phase were determined to be $a = 2.86$, $b = 0.943$, $c = 0.69$ nm in the orthorhombic system. It is yet unclear how much this phase affects the whole CDHA decomposition process.

The internal HAP/octacalcium phosphate (OCP) phase interface has attracted researchers' attention for many

years.[39,40] During hydrolysis, OCP is converted to HAP. Considering the type of matching (see, for example, Ref. 41), OCP may serve as the basis for recrystallizion to HAP. Presumably, HAP growth on OCP is involved in remineralization processes. Fernandez *et al.*[40] proposed an optimal model of the interface that corresponded to HRTEM images, which characterize its partial coherence in the presence of misfit dislocations with a period of $\sim$10 nm.

In relation to the development of reinforced bioceramics, TEM studies of the phase stability and microstructure of two-phase systems, *e.g.*, HAP – mullite system[42] having high hardness (up to 15 GPa), are being performed. As regards CP coatings, the vast majority of structural studies is limited to analysis of the phase composition, changes in the HAP crystal lattice parameters upon ion substitution (according to X-ray diffraction) and morphological organization [according to scanning electron microscopy (SEM)]. This is mainly due to requirements to the functional properties of bioactive coatings, which depend on the above parameters. In a discussion of the properties of phosphates[43] and coatings based on them,[44] an important role of dislocations has been noted; however, both theoretical and experimental data on the grain boundaries and interfaces should be considered insufficient.

The first results concerning dislocation structure of the grain boundaries in thin HAP coatings were reported by Ievlev *et al.*[32] Films of 50 – 100 nm thickness were applied onto unheated substrates (fluorophlogopite) by ion beam sputtering of a HAP ceramic target. The amorphous films thus formed were crystallized upon annealing in air at 700 °C for an hour. The phase composition of the films was determined by electron diffraction on an electron diffractometer. The grain size was in the range of 20 to 100 nm. No dislocations within the grains were identified by amplitude and phase contrasts.

The TEM images of structures of the film and the area covering the boundary between grains *1* and *2* are presented in Fig. 3. In grain *1*, planes $(21\bar{3}0)$ are resolved and in grain *2*, planes $(01\bar{1}0)$ and $(2\bar{3}11)$ are resolved. A periodic substructure as a series of dislocations is clearly seen along the boundary. The Moire period [the result of double diffraction on nearly parallel $(21\bar{3}0)$ and $(2\bar{3}11)$ planes in the grain superimposition area as the boundary is arranged at an angle to the image plane] is $\sim$2.4 nm and the Moire bands correspond to the positions of grain boundary dislocations. The calculation taking into account of misorientation of the reflecting planes being matched relative to the normal to the image planes showed that the identified series of dislocations counterbalances the size misfit

$$\frac{d_{21\bar{3}0} - d_{2\bar{3}11}}{d_{21\bar{3}0}} \approx 0.091$$

and misorientation ($\sim 6^\circ$) of the corresponding planes on the common high-angle boundary between grains *1* and *2*.

Studies of metal/coating interfaces focus on the metal interaction with CP and formation of compounds either increasing (or decreasing) the adhesive strength, the ways of modification of the metal surface by barrier layers, which suppress the diffusion of undesirable elements from the metal and increase the adhesive strength. As noted above,[2] in the biomimetic method for HAP application, titanium surface is oxidized to enhance biomineralization.

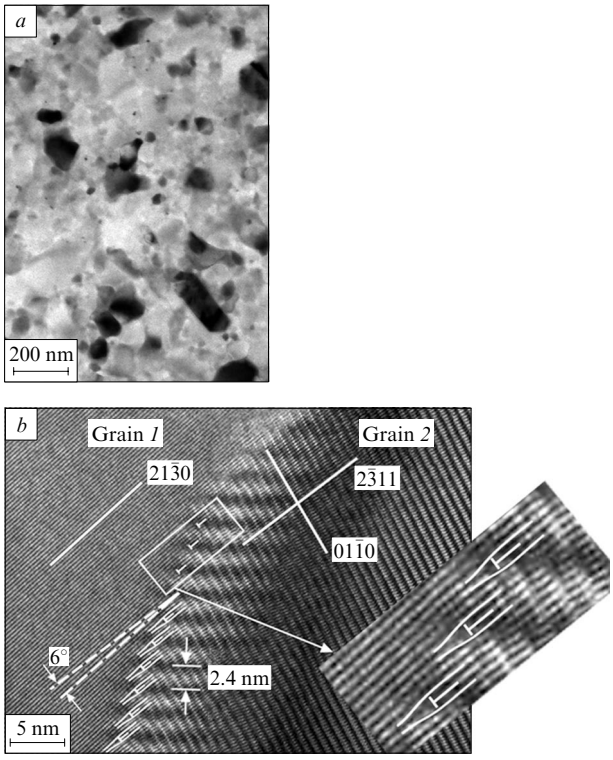


Figure 3. TEM images of the HAP film (*a*) and the area containing grain boundary (*b*).[32]

The adhesive strength of HAP coatings is increased by heat treatment, which activates the solid-phase interaction at the HAP/Ti interface giving simple (TiO_2)[45] and complex ($CaTiO_3$) oxides.[46] The interaction in the Ti – HAP system is under vigorous research in connection with adhesive strengthening and also in connection with the development of reinforced composite bioceramics based on this system.[47] In the latter case, the range of the resulting compounds is broader.

In some cases, the metal is precoated by an intermediate adhesion layer (ZrO_2,[48] mixtures of refractory metal oxides with phosphates[49]). Apart from oxidation, the corrosion resistance may be increased by applying passivating layers, for example, based on titanium nitride.[50] Note that available data on crystalline phase matching, atomic structure of interfaces and macrostresses in the metal – coating heterosystem are insufficient.

Since the formation kinetics of the mineral component (calcium phosphates) of bone tissue is substantially dependent on the content of impurity elements, in particular silicon, structural studies have been concentrated on the changes in the crystal lattice parameters of the silicon-substituted HAP[29,51] and distortion of the basic clusters — CP structural units.[52] Porter *et al.*[30] prepared single-phase Si-HAP by precipitation from an aqueous calcium- and phosphate-containing solution of Si acetate. According to X-ray diffraction data, for comparable Ca : P and (Ca + Si) : P ratios, the crystal lattice of Si-HAP tends to have smaller parameter *a* and greater *c*. An increase in the unit cell volume of Si-HAP was also noted and attributed to the PO_4 tetrahedron being larger than SiO_4. The increase in the biological activity was explained by impurity-induced

changes in the grain boundary structure (higher fractions of grain boundaries and triple junctions). Changes of this type mainly affect the solubility. Evdokimov *et al.*[53] attributed higher solubility of sulfate-substituted HAP to structural microdeformations introduced by the replacing ion due to different sizes of SO_4^{2-} and PO_4^{2-} anions.

The stimulation of bone tissue formation on zinc-doped CP ceramics was also attributed to distortion of the atomic structure.[52] Virtually all of the studies of the ion substitution effect were performed on ceramics. These results can be extended to coatings if specific structural features are taken into account. In particular, the substitution of silicon for phosphorus affects in the same way the crystal lattice parameters also in Si-HAP coatings formed by high-frequency magnetron sputtering.[54]

2. Crystal growth mechanism

The coating method undoubtedly affects the structural, substructural and morphological organization of coatings in various ways due to differences in process kinetics and the media where (or from where) the nucleation and growth take place.

Multiple two-dimensional mechanism for the nucleation and growth of HAP crystals from solutions was reported.[55, 56] The minimum thickness of two-dimensional HAP nanocrystals (0.82 nm)[56] and growth step heights (~0.8 and 1.6 nm) found by atomic force microscopy[57] on the minimum-energy prismatic face $\{10\bar{1}0\}$ provide reliable evidence for this mechanism. Proceeding from the height of growth steps and the presence of 0.7 – 1.0 nm CP clusters in the simulated body fluid (determined by dynamic light scattering), Onuma and Ito[58] concluded that the HAP growth unit may be represented as the Posner cluster $Ca_9(PO_4)_6$ (Fig. 4) the dimensions of which in the basis plane of the HAP crystal and along axis *c* are 0.815 and 0.67 nm, respectively; a growth model was proposed in the study cited. The comparison of the IR spectra of amorphous calcium phosphate (ACP) and crystalline HAP (positions of peaks for the vibrational modes of the PO_4^{3-} tetrahedra) performed in early works[60] attests to almost equivalent environments of phosphorus atoms), and the X-ray diffraction data for ACP (radial distribution of atoms)[59, 61] attest to the cluster structure of amorphous calcium phosphates. Apparently, clusters play a crucial role not only in the HAP crystal growth from solutions but also in the crystallization of amorphous coatings with a nearly HAP composition. It was noted[62] that crystallization may be a consequence of direct ACP → HAP transfer or the ACP → OCP → HAP transfer with the intermediate crystalline phase. Water was noted to activate the crystallization. From *ab initio* calculation data, a conclusion was drawn[63] about the existence of the $[Ca_3(PO_4)_2]_3$ clusters, which supports the idea of cluster organization of calcium orthophosphates. The layer-by-layer growth by the mechanism of direct cluster incorporation was substantiated by slow kinetics typical of molecular crystal growth.

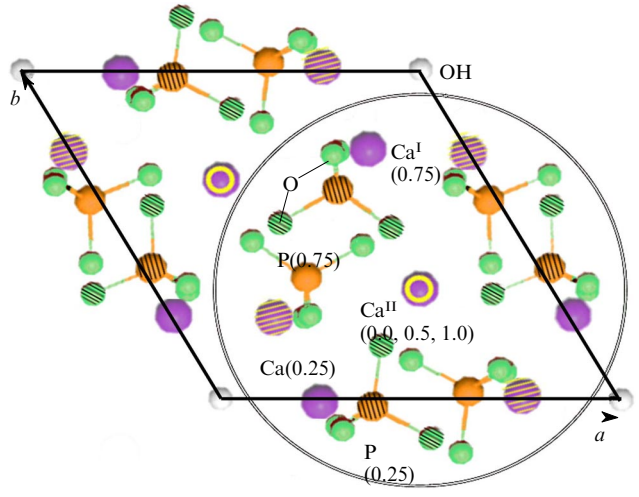


Figure 4. Posner cluster (marked by a circle).[59]
The coordinates of the corresponding atoms along the *c* axis of crystal lattice of HAP are indicated.

The relatively high-energy coating methods — plasma spray deposition, pulse laser ablation, ion beam and high-frequency magnetron sputtering — are characterized by high kinetic energy of flux components, uncertainty of the flux molecular composition even when the elemental composition is quite definite, the presence of ionized components and a flow of liquid phase microdrops, in particular, containing the remainder of the crystalline phase (for the first-mentioned method), and generally fast coating buildup kinetics (as compared with the biomimetic method). Therefore, for these methods, the considered mechanism is impossible and a high degree of non-equilibrium for coating growth and coating structure formation is predetermined. In view of this, the microscopic coating growth mechanism for these methods should not be considered as established. An advantage of the above methods is rather good reproducibility of the elemental composition of the precursor (powder, ceramics) in the condensed solid phase of the coating. This opens up the possibility to ensure crystallization of the amorphous phase *via* additional activation, because preparation of the final compound does not require component diffusion by large distances. However, it cannot be ruled out that even upon ion sputtering of the target, the flux contains clusters, *i.e.*, fragments of HAP molecules. At least, they were detected in a flux of thermally evaporated perovskites;[64] plasma used for ion ablation was found to contain molecular components apart from atoms and ions.[65] Since HAP has strongly bound groups, they may also exist in the condensed flux.

3. Requirements imposed on coatings

For performing the key function, bioactive adaptation of the implant, CP coating should meet a number of requirements on the composition, structure, morphology, mechanical properties and thickness, which in combination determine the body tolerance to the implant and the implant service life.

By the coating stability is meant not only the mechanical strength (especially in the initial stage) but rather the balance of the calcium phosphate dissolution and redeposition. The rates of these processes appreciably depend on the structures, being maximum for ACP and minimum for crystalline HAP. The dissolution of the CP coating is the key process that ensures the subsequent isolation and osteointegration of the bone-like apatite. The biological

activity considerably depends on the morphology of the surface coating: roughness and porosity increase the cell activity.[66] Higher-energy surfaces are more active; in the case of HAP, this is the (0001) surface. Thus, the formation of the appropriate coating texture is favourable, which has been demonstrated for HAP coatings obtained by high-frequency magnetron sputtering [54] and for biomimetic coatings originating on the (110) surface of titanium oxide (anatase).[67]

It is necessary to ensure both the mechanical (implant fixation) and chemical stability of the coating at the interface. The chemical stability is important, in particular, because the thickness of a coating determines the possibility for metal ions to penetrate into it, as was shown for the 90Ti6Al4V alloy.[68]

The question of the necessary thickness of a HAP coating may yet be regarded as open due to the pronounced dependence of its morphology on the way of application, the morphology ranging from compact structures with a nanorelief formed by high-frequency magnetron sputtering [69] to loose structures with highly developed surfaces and porous biomimetic precipitates [70] the thickness of which can be estimated only by dividing the total volume by the surface area being coated. The choice of the coating thickness with allowance for resorption depends also on its atomic structure (amorphous or crystalline), the degree of dispersion of the grain structure and phase composition. The coating thickness is also limited by the technological characteristics of their preparation such as very slow synthesis in biomimetic processes (latent period before the formation of the HAP crystalline phase is 28 days),[71] relatively low growth rate (several nanometres per second) in the case of high-frequency magnetron or ion beam sputtering of ceramic targets and high output for plasma spray deposition (~ 10 μm s^{-1}).

The biochemical processes occur upon interaction of the physiological medium with the surface layer of the coating; nevertheless, when choosing the coating thickness, it is also necessary to consider the coating stability and good adhesion to metal. In particular, considering the stability in the physiological medium and adhesion at the interface with titanium, a coating thickness of 10 μm was established.[72] However, in view of the considerable dependence of the phase composition, structure and morphology of the coating on the deposition method, a particular thickness may be chosen only in each particular case.

The expediency of using very thick coatings has not yet been substantiated from the biological standpoint. As regards structural and morphological features, due to porosity, which develops as the thickness increases up to large values, the cohesion strength decreases, resulting in disintegration within the coating.[73] The adhesion and cohesion strength of the coating should be at least no less than that of the human bone (18 MPa), in view of the fact that the metal/coating interface is the first to be destroyed upon long-term implantation

III. Deposition of calcium phosphate coatings

1. Biomimetic hydroxyapatite coating

Recent years have seen enhanced interest of researchers in biomimetic [15] synthesis of HAP on the surface of titanium implants from aqueous solutions simulating body fluids.[74] Below is given an example of the composition of such fluid.[75]

Ion	Na^+	K^+	Mg^{2+}	Ca^{2+}	Cl^-	HPO_4^{2-}	SO_4^{2-}	NCO_3^-
Content / mmol litre^{-1}	142.0	5.0	1.5	2.5	148.5	1.0	0.5	4.2

The advantages of the method include simple technology, the possibility of uniform coating of a surface of any shape, relatively low temperature (close to the body temperature), the possibility of ion substitution and insertion of medicaments or biomolecules in the course of coating buildup.

The rate of HAP nucleation and the morphology of surface coatings depend on the surface activity; in the case of titanium implants, this is related to Ti – OH groups. For this purpose, the surface is treated with water vapour [76] or with a boiling solution of $Ca(OH)_2$ (Ref. 77) or is immersed into NaOH. In the latter case, sodium titanate and titanium oxide are formed, which are hydrolyzed in the simulated body fluid to give negatively charged hydroxyl groups. The OH groups collect calcium ions, which in turn collect phosphate ions. Crystalline apatite appears after 28 days.[71]

The activity increases in the presence of a titanium oxide film, which is hydroxylated and, hence, ensures high density of apatite nucleation.[78] The first and the principal stage of this process is the formation of Ti – OH groups. It was shown [67] that the activities of amorphous and crystalline oxides are different; however, the structure is not the crucial factor. A more important role belongs to lattice matching at the HAP/metal oxide interface: the activity difference is explained by the fact that not all of the Ti – OH groups can be effective in HAP nucleation but only the particularly oriented groups.[79, 80] The orientation and the surface density of hydroxyl groups predetermine the dependence of the nucleation probability and morphological forms of growth of a HAP coating on the type of TiO_2 crystal lattice and the crystallographic plane that forms its surface. Anatase is more active than rutile; specifically, the (110) plane of anatase (A), which is favourable for the epitaxial growth of HAP with an orientation relationship with anatase (0001),[$2\bar{1}\bar{1}0$]HAP||(110),[001]A when the size misfit of the basis vectors of lattices with nearly coinciding sites does not exceed 0.02 (Fig. 5 *a*). Moreover, the Ti – OH groups formed on the (110)A surface match well the (0001) plane of HAP, which ensures its oriented nucleation.[81]

Considering the possibility of good lattice matching at the interface, Lindahl *et al.*[82] investigated the character of HAP growth on the (100), (110) and (001) planes of rutile (R). Better 'wettability', *i.e.*, HAP nucleation as a dense layer of (0001) orientations is characteristic of coatings on the (001)R plane. The 'wettability' on (100) and (110) surfaces is poorer to different extents; as a result, spherical porous concretions of many thin HAP crystals are formed in the initial stage. The observed morphological features for surfaces of different orientations are quite understandable. The highest surface energy for the (001)R orientation (σ_1) ensures the layer-by-layer nucleation and coating growth even for a sparse lattice of matching sites at the (001)R/(0001)HAP interface (Fig. 5 *b*)

$$\sigma_{(001)TiO_2} > \sigma_1 + \sigma_{12} + \sigma_3$$

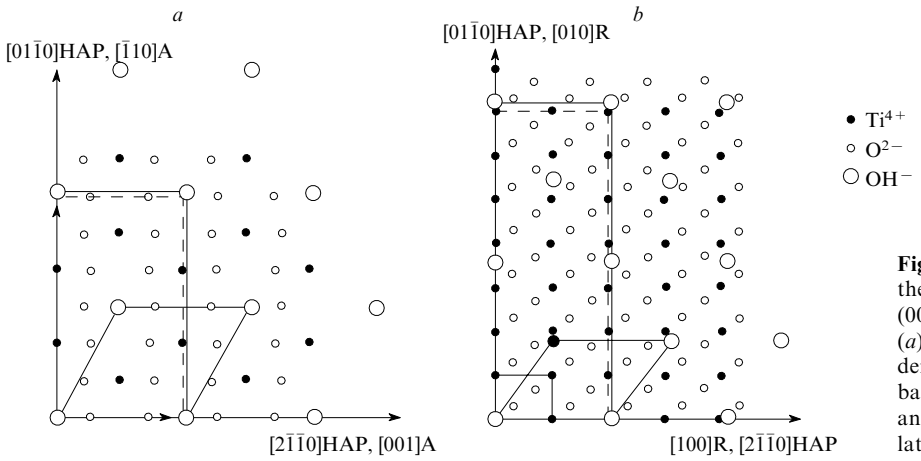


Figure 5. Coincidence site lattices at the (110)A/(0001)HAP (*a*) and (001)R/(0001)HAP (*b*) interfaces.
(*a*) The basises of two equivalent coincidence lattices are marked out; (*b*) the basis cells of the HAP and rutile lattices and the basis of the coincidence site lattice are distinguished.

Here σ_2 is the energy of the free surface, σ_{12} is the interface energy, σ_3 is the elastic deformation energy caused by the size misfit of the coincidence site lattice in the coordinates of the initial crystal lattices of rutile and HAP ($\leqslant 0.02$). The [0001]HAP texture on the (001)R surface is specified by the parallel arrangement of [100]R and [2$\bar{1}\bar{1}$0]HAP directions of the lattices being matched and by matching of the required planes at the interface.

For the (110)R surface, which has the minimum energy, the inequality sign is reversed and HAP nucleation is discrete.

Despite the good matching at the (101)R/(0001)HAP interface, a discrete HAP nucleation should also be expected on the (101)R plane because it corresponds to a relatively low-energy surface. In particular, twinning in the rutile phase formed upon titanium oxidation occurs on the (101) plane,[35] which also implies that it is a low-energy surface.

On all the studied surfaces, transition from the nucleation texture to the growth texture can be noted: on the (001)R surface, this is transition from the normal [0001]HAP texture to a pronounced deviation from the normal to the surface; on the (110)R surface this is transition to the [10$\bar{1}$0] texture. The HAP grains on the (100)R surface are randomly oriented. The signs of epitaxy at the early stage promote HAP adhesion for (100) and (110) surfaces of rutile but to a greater extent for the (001) surface. The real structure of titanium oxide depends on the oxidation technique, and the orientation of the free surface in the topochemical synthesis is determined by the orientation relationships between the crystal lattices of titanium and TiO_2.[35,83] Therefore, predominant orientations of the oxide surface can be predicted only for known textures of the surface layers of a titanium item. Otherwise, the heterogeneity of the properties of the oxide surface should affect the general morphology, the adhesive and cohesive strengths and biochemical properties of the HAP coating. Therefore, a highly dispersed nanocrystalline structure of titanium and, correspondingly, titanium oxide is preferred. The formation of such structure is facilitated by rutile chemoepitaxy in several equivalent orientations, which is implemented even in single-crystal titanium.[83]

2. Electrochemical and electrophoretic deposition

Among the solution techniques for HAP coating, the techniques based on substance electrotransfer, in particular, electrochemical cathodic deposition and electrophoretic deposition can be considered rather convenient.[15] The advantages of electrochemical deposition are the process temperature not exceeding 100 °C, the possibility of coating profiled parts and the control over the coating morphology attained by changing the current density; the drawbacks are relatively low adhesive strength, which decreases upon increase in the current density, the need to stabilize the HAP phase, the morphological inhomogeneity, which is manifested as large (several micrometres) laminated aggregates being formed on the surface.[84] To increase the adhesion, accelerate the deposition and, hence, increase the degree of dispersion of the nanocrystalline HAP coating, Shalaby *et al.*[7] formed preliminarily an ordered system of nanopores on the surface of the Ti6Al4V alloy. Upon heat treatment, the porous oxide was converted to anatase.

By electrophoretic deposition, it is possible to form a gradient coating having a dense layer; such coatings have good adhesive strength and are transformed into porous less stable structures.[85] The subsequent heat treatment at 800 °C for sintering of the coating is required. An approach for increasing the adhesive strength by creating composite layers was proposed.[86] The composite coating deposited on titanium or the Ti6Al4V alloy contained [TiN + Ti_2N + α-Ti(N)] and ($SiO_2 - TiO_2$) intermediate layers followed by an electrophoretically formed thin homogeneous bioactive external HAP layer. The intermediate layers were prepared by glow discharge nitriding in a plasmotron and by the sol–gel method, respectively. The structures of the coatings produced by these methods are little studied.

3. Sol–gel process

A simple method for deposition of relatively thick homogenous porous HAP coatings is based on the sol–gel process.[87] The phosphate precursors used to synthesize HAP are P_2O_5,[88] $P(OEt)_3$,[89,90] H_3PO_4 [89] and $(NH_4)_3PO_4$,[91] while the calcium precursors are $Ca(NO_3)_2 \cdot 4H_2O$,[89,91] $Ca(NO_3)_2$ [92] and $(AcO)_2Ca$.[90,93] The conditions of synthesis and product characteristics will be illustrated by considering the reaction between the first of the listed precursors:

— ethanol solutions of P_2O_5 (0.5 mol litre^{-1}) and $Ca(NO_3)_2 \cdot 4H_2O$ (1.67 mol litre^{-1}) in ratio Ca : P = 1.67 are mixed in the corresponding HAP;

— the mixture is stirred (24 h) until a white gel is formed;

— the gel is dried at 80 °C (24 h);

— the product is heated in air to 600 °C at 5 °C min^{-1} and kept at this temperature for 6 h;

— the product is cooled in air to room temperature.

As a result, only the nanocrystalline HAP phase is detected. When annealing is carried out at 700 °C in the same mode, β-calcium phosphate and CaO phases resulting from partial decomposition are added,

$$Ca_{10}(PO_4)_6(OH)_2 \longrightarrow 3\,Ca_3(PO_4)_2 + CaO + H_2O$$

Note that the crystalline HAP phase was detected only after the annealing at 600 °C. In some experiments, lower temperatures (down to 350 °C) of sol – gel HAP synthesis were noted; this was due to the presence of water in the gel phase. The nanodispersed structure formed in this process promotes high biological activity,[94] while relatively low density of the coatings and open porosity of the coatings enable the circulation of biological flows. The main drawback of these coatings is low adhesive strength. To increase it (and to increase the corrosion resistance), an oxide layer with up to 200 nm thickness is formed on the metal.

Despite the simple technology, this method has not become competitive with the plasma spray deposition as regards the process duration and the achieved parameters, first of all, strength characteristics.

4. Plasma spray deposition

The deposition of the interaction products of CP powder particles with low-temperature plasma from a plasma gas flow is the key highly productive method used for the formation of thick (up to 200 – 300 μm) coatings on metallic implants. The engineering aspects of the process have been reported.[16, 95, 96] The advantages of the method include the possibility to deposit a coating of any reasonable thickness at a high rate (up to 10 μm s^{-1}), fairly high adhesion (caused by the presence of charged particles in the deposited flow) and the possibility to control the coating porosity by changing the mode and the degree of dispersion of the powders introduced in the plasma.

The features of the process are as follows: plasma temperature, $\sim 10^4$ K; inhomogeneous composition of the flow condensed onto the implant, ranging from single atoms to microdrops, fast (10^6 K s^{-1}) cooling of which yields metastable (including amorphous), morphologically and structurally inhomogeneous phases; and deviation from the elemental composition of the initial powders caused by the loss of volatile components. The influence of the amorphous phase on the properties of the coating depends on its location, namely, being located in the surface layer it promotes growth of the bone tissue due to higher bioresorption,[97] while in the vicinity of the Ti/CP interface, fast dissolution of the amorphous phase leads to a decrease in the adhesive strength and peeling off of the coating before the bone tissue has formed. Therefore, with the general regularities being the same, the quantitative estimates of the properties of coatings formed by this method may be different in different studies.

In an early systematic study of plasma coatings obtained by plasma spray deposition, it was shown [46] that spraying is accompanied by complete dehydration to give oxyapatite in which half of the OH sites every two lattice periods are substituted by oxygen atoms, while the other sites remain vacant to preserve the charge balance. As regards the amorphous phase, for decreasing the solubility and enhancing the cohesive and adhesive properties of the coating, its complete crystallization followed by heat treatment are required. This activates the chemical reactions of CP with the metal. The heat treatment above 700 °C in a dry atmosphere leads to crystallization to give oxyapatite.

The crystal lattices of oxy- and hydroxyapatite differ by the parameter *c*, which can be noted by a slight shift of the diffraction peaks to smaller angles for oxyapatite with respect to HAP. The annealing of the amorphous phase in the atmosphere of saturated water vapour induces crystallization at $\sim$500 °C, while at 600 °C, the hydroxyl groups actively diffuse during crystallization (activation energy 230 kJ mol^{-1}) into areas depleted in these groups. The introduction of hydroxyl groups leads to weight gain. According to thermogravimetric analysis, the weight increases by 2.3%, which corresponds to 67% occupancy of the sites (for total occupancy the weight gain should be 3.4%). The heat treatment at 700 °C results in complete crystallization of the amorphous phase in oxyapatite, while high-temperature treatment gives rise to $CaTiO_3$ at the interface, which is formed upon the reaction of TiO_2 with CaO *via* the non-equilibrium intermediate phase $CaTi_2O_5$.[44]

The coating morphology and adhesion were found [98] to depend on the particle size of the initial powders forming from a laminar flow of high-power plasma ($\sim$52 kW) at different substrate temperatures (15 to 200 °C) and different distances to the substrate (L = 80 – 150 mm). It was found that a 20-fold change in the weight of powder particles has a considerable effect on the morphology, phase composition and adhesion of the coatings. The coatings containing more than 90% of crystalline phases (the major phase was HAP and traces of β-calcium phosphate and CaO were present) were formed from fine powders (particle size 33 μm) at L = 80 mm and from coarse powders (particle size 90 μm) for the whole range of L values studied. When L = 150 mm, the content of ACP in the finer powder coating substantially increased. As the temperature was raised from 15 to 200 °C, the fraction of ACP in the finer powder coating decreased from 46% to 36%, while that in the coarser powder coating increased from 4% to 11%. The adhesive strength of the 300 μm-thick coating prepared from the finer powder was 54 – 56 MPa. For the 125 μm-thick coating prepared from the coarser powder at 200 °C, the adhesive strength exceeded 60 MPa. As the coating thickness increased, this parameter decreased with the increase in the substrate temperature to reach a constant value at 100 °C.

Apart from heat treatment, the adhesive strength may be increased by application of intermediate layers, in particular, ZrO_2,[48] and by forming a gradient structure in which the highly adhesive HAP layer is formed upon ion-stimulated deposition.[99]

The possibility of forming the coating texture has been studied by Tong *et al.*,[100] who demonstrated the increase in texturing along the [0001] direction with the increase in thickness. This is related to the temperature gradient and possibly to the geometric selection principle involved in the growth of thick coatings.[101] The shape anisotropy with the predominant [0001] direction is well manifested even in the synthesis of nanopowders.[25, 26] Since the smallest habit face (0001)HAP is least sensitive to dissolution,[102] by varying the degree of texturing, it is possible to control the resorption of coatings.

The coating morphology has a rough relief caused first of all by the presence of drops of different size in the flux.

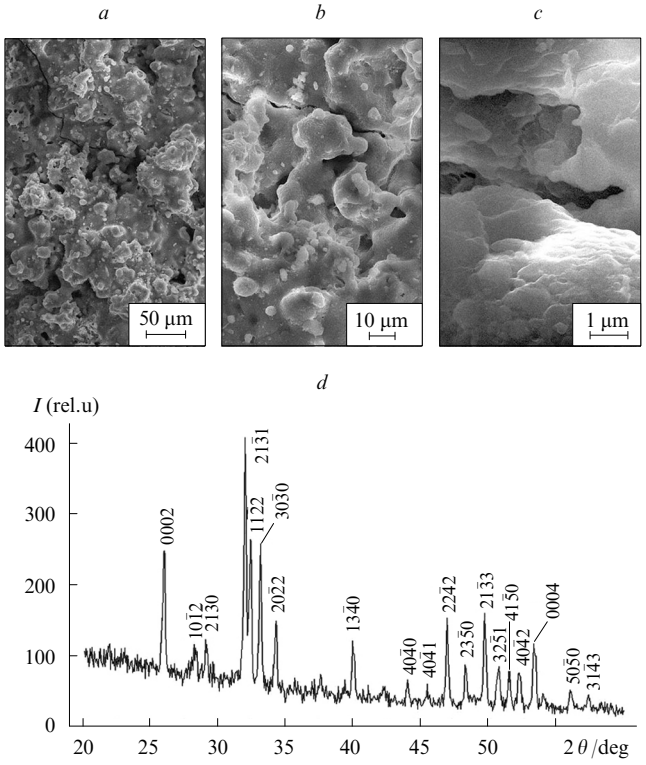


Figure 6. SEM images of the surface of thick (~200 μm) HAP coating on titanium (*a* – *c*) on different scales and X-ray diffraction pattern of this sample (*d*).

Figures 6 *a* – *c* show the SEM images characterizing the morphology of a CP coating‡ with thickness of ~200 μm deposited on titanium from a HAP powder with a particle size of 25 – 60 μm heat-treated for 1 h at 650 °C in a water vapour medium. The images on different scales show the relief at different levels, open microporosity and extended fractures, which can be due to difference between linear thermal expansion coefficients of HAP and titanium, 14 and 8.5×10^{-6} deg^{-1}, respectively.[103]

The possibility of diffusion 'healing' of the surface is limited by the low mobility of strongly bonded phosphate groups. The porosity, rough relief and structural and morphological heterogeneity of the surface hamper estimation of hardness of the coatings by nanoindentation (the results are highly scattered). A detailed study of 230 μm-thick microplasma coatings demonstrated[104] a clear-cut indentation size effect, characterized by increase in the hardness (H) following a decrease in the load (P); the H value varied from 5.0 to 1.5 GPa and the Young's modulus (E) varied from 100 to 60 GPa for indentation depths from 170 to 3000 nm. This effect is manifested in various materials,[105] but it may be of different nature and different factors are taken into account for interpretation.

Dey *et al.*[104] interpreted the observed trend as the contribution of spatial defects (pores, microfractures), correlating their number with the indentation volume and considering the fact that defects reduce the contact area. Without separating the true indentation size effect from the influence of spatial defects, the observed trend has also been attributed to the increase in the spatial density of fractures at great penetration depths of the indenter and accompanying decrease in the contact area.

The trend in question was confirmed by a nanoindentation study[106] using the procedure proposed in another publication[107] of the hardness of samples, the surface morphology of which is illustrated by Fig. 6 *a* – *c*. The phase composition is characterized by the X-ray diffraction pattern shown in Fig. 6 *d*, indicating that the crystalline phase of the coating is presented by hydroxyapatite, and the background level in the low-angle region attests to a small fraction of the amorphous phase. This is also supported by TEM images of coating cross-sections. It follows from $P-h$ diagrams where P is the specified load, h is the indenter penetration depth (Fig. 7), and data of Table 2 that at different degrees of deformation, hardness decreases with increase in the load. A three- or four-fold scatter of the H values at any load reflects the structural and morphological heterogeneity of the coating surface observed by SEM and by atomic force microscopy. TEM image of cross-section fragments characterizing the grain structure of the coating are shown in Fig. 8. Analysis of dark-field TEM images showed that the size of coarse HAP grains is 0.1 – 0.4 μm; these are agglomerated nanograins with a minimum size of up to 5 nm glued together by the amorphous phase. The kinks in the loading diagrams (see Fig. 7) are due to the indenter reaching the internal porosity of the coating. Therefore, it was stated[104] that studies of the variation of hardness and elastic modulus *vs.* load by nanoindentation should employ the Weibull statistics.[108]

The considered examples demonstrate that hardness certification of such coatings by nanoindentation is still

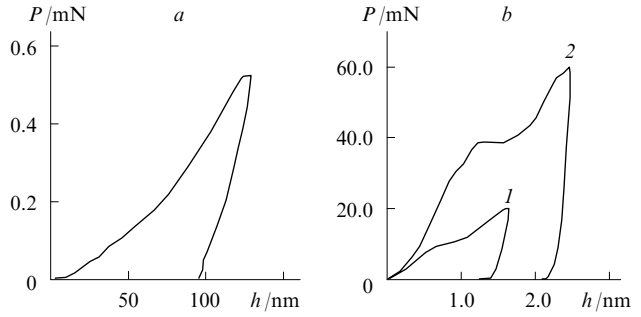


Figure 7. Indentation depth vs. load.[106]
P_{max} = 0.5 (*a*); 20 (*1*) and 60 (*2*) mN (*b*).

Table 2. Hardness of the 200 μm-thick coatings from the nanoindentation results (the mean values of at least six measurements are given).[106]

P_{max}/mN	H_{min}/GPa	H_{max}/GPa	H_{mean}/GPa (see [a])
0.5	1.2	3.2	1.8
20.0	0.2	0.8	0.5
60.0	0.2	0.6	0.4

[a] The mean value of several measurements.

‡ The sample for investigation was provided by V I Kalita (A A Baikov Institute of Metallurgy and Materials Science of the Russian Academy of Sciences).

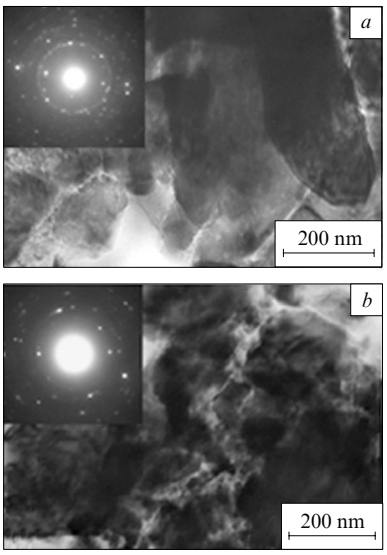


Figure 8. TEM images and microdiffraction patterns (in the insets) of cross-section fragments of the plasma spray deposited coating on titanium.

problematic. The mechanical properties are improved when not only hydroxyapatite coatings are plasma spray deposited but also composite coatings, in particular, HAP – ZrO_2 [109] and HAP – Ti.[70] In the former case, a 90% content of the crystalline phase was attained, and up to 50% ZrO_2 content in the coating did not affect considerably the HAP decomposition.

5. Pulsed laser ablation

The pulsed laser ablation technique is studied in relation to the possibility of fast deposition of thin (several micrometres) CP coatings. This method is characterized by high particle flow density (up to 10^{20} cm^{-2} s^{-1}) and, hence, high condensation rate (0.01 – 1.0 Å per pulse);[110] a kinetic energy of particles in the flux of 10 – 200 eV; the presence of drops in the flux resulting from the laser vaporization mechanism according to which the accelerated ($> 10^6$ cm s^{-1}) flux is formed from plasma arising upon laser beam interaction with the surface of the target (for the specific laser radiation power of $10^8 – 10^9$ W cm^{-2}, the plasma temperature is 10^4 K). These features predetermine the structure and properties of the coating: amorphous phase, high hardness and adhesive strength and reproduction of the initial elemental composition of the target in the coating. The substance transfer with retention of the composition is due to high heating rate of the target in the laser spot area and thermal ablation. The limitations on the possibility to retain the same composition are related to the laser spot size and the angular distribution of components in the flux.

On unheated metal, amorphous coatings are formed.[110, 111] The extensively developed surface morphology [103] is a consequence of the drop mechanism of coating growth with a broad range of drop sizes — from a tenth of a micrometre to several micrometres. Since the solubility of amorphous coatings is high, their crystallization requires heating of the substrate to $T > 400$ °C under water vapour during or after the deposition. A study of structure variation *vs.* water vapour pressure during the growth demonstrated [112] that the pressure buildup induces the formation of pores. As in the other methods used to examine the adhesive strength of coatings, here also the problem of oxide formation on the metal surface is faced.

Nelea *et al.*[113] studied the stimulating effect of UV radiation from a mercury lamp on the formation of 0.5 – 2.5 μm-thick coatings at room temperature on the TiN/Ti5Al2.5 Fe heterojunction structure upon pulsed KrF laser-induced (248 nm) ablation of the crystalline target made of pure (99.98%) HAP. After deposition, the coating was annealed in air at 500 – 600 °C. The TiN barrier layer was also deposited by laser ablation of stoichiometric TiN under nitrogen (10^{-1} Pa) at a substrate temperature of 550 – 650 °C. The UV-stimulated film growth occurred in an oxygen atmosphere ($10^{-2} – 10^{-1}$ Pa) directly on the Ti5Al2.5Fe alloy at 500 – 600 °C. The considered approach relies on activation of oxygen reactivity upon photodissociation of the dioxygen molecule and formation of ozone.

Comparative characteristics of the coatings obtained by pulsed laser ablation either with or without UV radiation demonstrated the increase in the hardness from 2.5 to 7.0 GPa, a 2.5-fold smoothing of the surface relief, a change in the Ca : P ratio from ~1.73 to 1.9 – 2.1 and a change in the phase composition (in addition to HAP, calcium pyro- and β-phosphate phases and CaO were detected). The latter changes are attributed to UV-stimulated partial decomposition of HAP with water loss from the target and plasma

$$Ca_{10}(PO_4)_6(OH)_2 \longrightarrow$$
$$\longrightarrow H_2O\uparrow + Ca_4O(PO_4)_2 + Ca_2P_2O_7 + 4\,CaO + P_2O_5\uparrow$$

The possibility to attain high hardness of the coatings upon pulsed laser ablation with sharply different structures of the 90HAP – 10FA target and the coating was demonstrated.[44] The results of the comparative studies of the morphology and mechanical properties (nanoindentation) of thin (1.2 μm) coatings formed by laser ablation and high-frequency magnetron sputtering were reported.[18] The difference between the hardnesses of the coatings at average coating thickness attained was found to be insignificant but for pulsed laser ablation, hardness was found to depend on the process parameters, in particular, on the dynamic pressure.

The advantages of laser ablation over plasma spray coating are as follows: during the growth, more homogenous, mainly amorphous structure is formed (high adhesive strength on unheated substrates, for example, 58 MPa [14]). The general characteristics of the coatings deposited by pulsed laser ablation are the following: 1 – 3 μm thickness; amorphous or amorphous-crystalline structure; a Ca : P ratio from 1.69 (Refs 112 and 114) to 3.72 (Ref. 110); a nanoindentation hardness of 3.48 ± 0.49 to 7.0 GPa;[113] and adhesive strength of 2 to 3 N.[110]

6. Ion sputtering

Two modifications of ion sputtering are mainly considered, high-frequency magnetron and ion beam sputtering; they have similar mechanisms but differ considerably in the medium in which the coating is formed, and this affects the coating structure. In both modifications, the sputtering mechanisms ensure good reproduction of the elemental composition of the target in the coating. High-frequency magnetron sputtering is best suited for deposition of films of dielectric materials, in particular, complex oxides.[115]

Thin (several micrometres) CP coatings obtained by these methods are widely investigated in connection with the possible preparation of compact amorphous structures by ion beam sputtering or amorphous, mixed amorphous-crystalline and nanocrystalline coatings by high-frequency magnetron sputtering. In the latter case, specified structures with high mechanical properties can be obtained without additional heat treatment and their resorption and biological activity can be controlled.

Starting from the first works on high-frequency magnetron sputtering of HAP, the CP coatings formed on unheated substrates have been certified as amorphous [116] or containing various amounts of the crystalline phase.[117] Pichugin *et al.*[118] attributed the formation of crystalline phases to the increase in the high-frequency discharge power; note that apart from crystalline HAP, the coating contained calcium pyro- and β-phosphates and CaO. Hong *et al.*[119] explained the formation of only crystalline HAP by the too low power of the high-frequency discharge, which does not suffice for decomposition of the HAP target. For amorphous coatings scratch testing revealed the dependence of adhesion on the coating thickness on commercially pure titanium:[116] the critical loads for 0.1, 1.0 and 4.0 μm-thick initial films were 15.70, 12.03 and 6.37 N; after a 2-h heat treatment at 500 °C, these values were 13.77, 10.50 and 1.60 N, respectively. The heat treatment resulted in complete crystallization of 0.1 μm-thick films and in partial crystallization of thicker films. After crystallization, the solubility in the simulated body fluid sharply decreased.

The threshold temperature for the formation of the ACP coating with minor crystalline inclusions of CaO was determined.[50] The Ca : P ratio was in the 1.73 – 1.78 range, *i.e.*, it was rather similar to this ratio in stoichiometric HAP. The structure, composition, morphology and hardness of HAP coatings on the Ti5Al2.5Fe alloy were studied in the presence and in the absence of a TiN layer between HAP and the metal. This layer serves to preclude the diffusion of atoms from the titanium substrate into the coating, and thus eliminates the possibility of formation of titanium oxide, which often reduces the adhesive strength at the interface [in some cases, however, the adhesive strength may conversely increase (see, for example, Ref. 45)]. The hardnesses of the coatings with and without the intermediate layer estimated by nanoindentation at a 10 nN load are nearly equal for both options ($H \approx 5$ GPa, $E \approx 150$ GPa) and is 1.5 times lower without TiN (at 0.5 nN).

Ievlev *et al.*[120] succeeded in the synthesis of compact nanocrystalline HAP coatings by high-frequency magnetron sputtering and elucidated the dependence of their structure on the spatial arrangement of the substrate, either above the erosion zone of the target or beyond this position. In the former case, single-phase nanocrystalline structures were formed on the unheated substrate,§ while in the latter case, the coatings were amorphous-crystalline or mainly amorphous, and their crystallization required the subsequent treatment. This difference was attributed to the spatial inhomogeneity of the plasma discharge and to different impacts of plasma components on the growth process.

The X-ray diffraction pattern of the 1.0 μm-thick HAP coating grown on unheated titanium plates is shown in Fig. 9 *a*. The well distinguished reflections correspond to nanocrystalline HAP. Analysis of the morphology of the cross-section chip of the coating (Fig. 9 *b*) showed the integrity of the grain structure (the absence of pores or fractures). A high-resolution TEM study of cross-section samples of HAP(2 μm)/Ti heterojunction structures confirms the formation of the nanocrystalline compact structure of the coatings. The light-field image of an area around the Ti/HAP interface, the corresponding microdiffraction pattern and a fragment of the isolated area in the plane resolution mode of the HAP crystal lattice are presented in Fig. 10. It can be seen that the interface is clear, has no exfoliations, micropores or titanium and HAP interaction products (see Fig. 10 *a*). No amorphous regions are present within the area of the HAP layer cross-section (see Fig. 10 *b*). Crystallographic planes of HAP are distinguished in the image: (0002) ($d = 0.344$ nm), $(21\bar{3}0)$ ($d = 0.308$ nm) and $(21\bar{3}1)$ ($d = 0.281$ nm), which belong to nanograins with 3 – 15 nm size (see Fig. 10 *c*). The Moire bands imply that within the cross-section thickness (tens of nanometres), the areas are not single-crystalline.

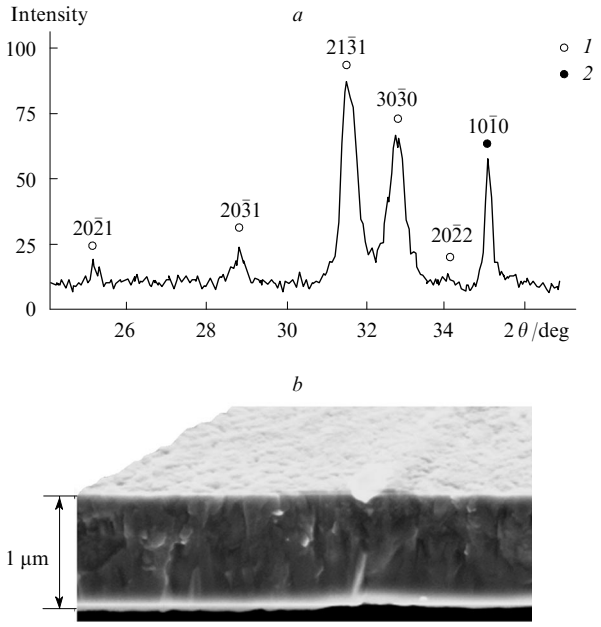


Figure 9. X-Ray diffraction pattern of a 1.0 μm-thick HAP coating grown above the erosion zone of the target (*a*) and SEM image of the cross-section chip (*b*).[120]
(*1*) HAP, (*2*) Ti.

The TEM images of areas of nanocrystalline and amorphous-crystalline films are shown in Fig. 11. It can be seen that there are no dislocations inside nanograins and that the grain boundaries contain no amorphous phase. As shown above, the grain boundaries of nanocrystalline films obtained by crystallization of amorphous phases were found to have regular short-period series of dislocations (see Fig. 3 *b*).

The concentration profiles of the major elements present in 0.1 and 1.0 μm-thick coatings from Auger electron spectroscopy with layer-by-layer ion beam sputtering of samples are presented in Fig. 12. The average Ca : P ratio for the whole bulk of a thin coating is 1.86 ± 0.10; in the vicinity of the interface, it increases to 1.94, while in the

§ The maximum temperature of substrate heating by plasma components during deposition of thick (1 – 3 μm) films was 350 °C.

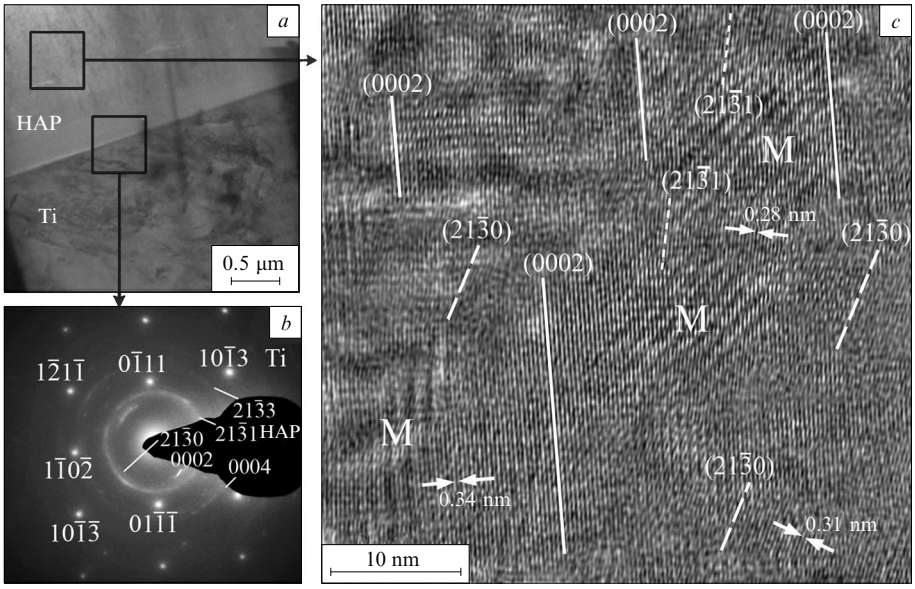


Figure 10. Cross-section view (*a*), microdiffraction pattern (*b*) of the Ti/HAP heterojuncion structure and high-resolution cross-section view of the HAP/coating structure (*c*).[120] M are Moire bands.

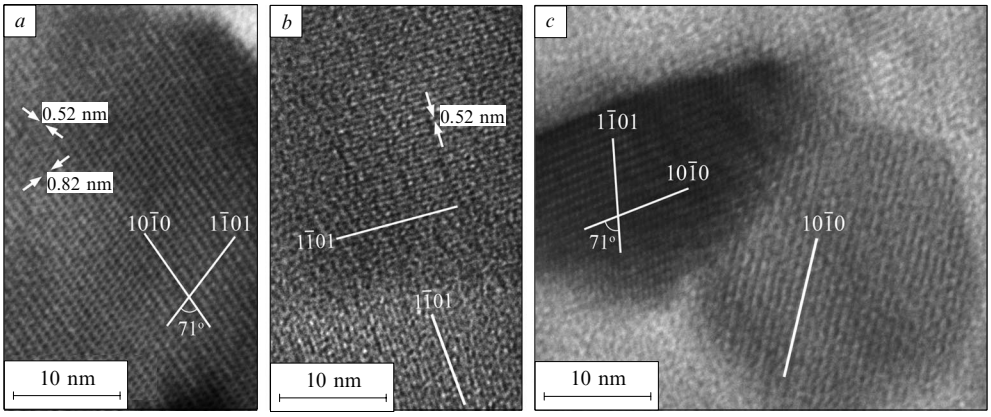


Figure 11. TEM images of areas of nanocrystalline (*a*, *b*) and amorphous-crystalline (*c*) HAP films.[69]

middle of the thickness (1.76) and in the surface layer (1.66) it approaches the stoichiometric value. The distribution pattern of the element concentrations for a thin coating is the following: for the whole bulk, the average Ca : P ratio is 1.85 ± 0.45, and on moving from the surface to the interface it increases from 1.38 to 2.35. The contents of oxygen (0.61 ± 0.01) in thin and thick coatings are nearly stoichiometric. An increase in the Ca : P ratio is also typical of coatings obtained by high-frequency magnetron sputtering [118] but in this case, it is not so pronounced.

The results of elemental analysis along the depth of an HAP coating on silicon performed by $^4He^{2+}$ Rutherford backscattering are summarized in Table 3.[37] The data of the Table are well correlated with the Auger spectroscopy data on the calcium, phosphorus and oxygen contents and also demonstrate that the hydrogen content in the coating bulk corresponds to the molecular composition of HAP. The monotonic decrease in the hydrogen concentration on approaching the HAP/Ti interface may indicate that on contact of the samples with air, the hydroxyl groups are formed.

The ultra-soft $L_{2,3}$ X-ray emission spectra of phosphorus for 0.1 μm-thick HAP coating supported on titanium and a stoichiometric HAP powder are presented in Fig. 13. The spectra were interpreted in the dipole approximation using the theoretical calculations of full and partial density of states for HAP in terms of zonal and cluster models. In this approximation, the spectral features designated by letters A' and A correspond to the subvalent 2s states of oxygen and 3s states of phosphorus hybridized with them. Points B' and B correspond to the major density maximum of the phosphorus 3s states, and C, C', C'' correspond to the partial contribution of the phosphorus 3s states to the valence subzone of the 2p states of oxygen. Owing to the latter fact, the C, C' and C'' maxima of the $L_{2,3}$ spectrum of phosphorus would be greater, equal to or considerably smaller than the principal peak of the 3s states of phosphorus depending on the degree of stoichiometry of compounds. The tails of the spectra at 130 – 132 eV are related

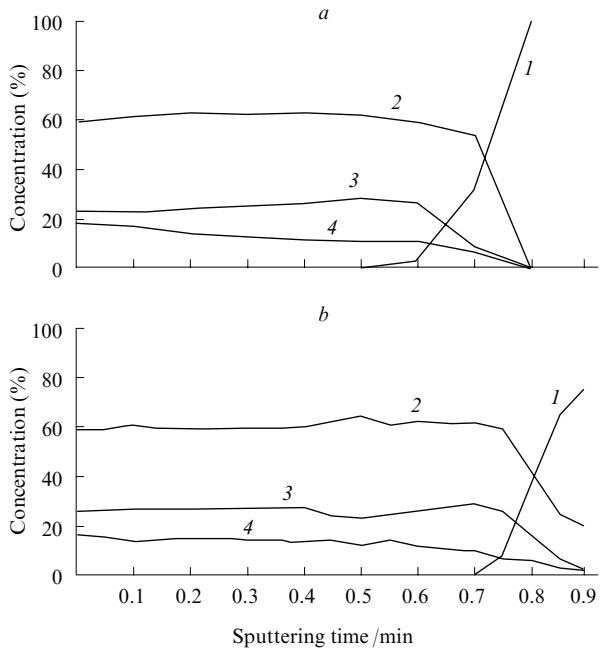


Figure 12. Concentration profiles of the major elements of HAP coatings with thickness of 0.1 (*a*) and 1.0 μm (*b*) on titanium.[37] Element: (*1*) Ti, (*2*) O, (*3*) Ca, (*4*) P.

to the s states of hydroxyl hydrogen. For the stoichiometric HAP, the $B:C$ ratio is 1. For the spectrum of a thin sample, the $B:C$ ratio is 0.97, which may attest to minor deviation from the stoichiometry. It is noteworthy that the spectra of non-annealed HAP samples both on titanium and on silicon exhibit some tails corresponding to the density of states at 130 – 132 eV, indicating the presence of hydroxyl groups.

For IR-spectroscopic studies, 1.0 μm-thick coatings were deposited on the surface of (111)Si and (111)CaF_2 single crystals.[120] The spectrum shown in Fig. 14 corresponds to nanocrystalline HAP, the bands being due to PO_4^{3-} on CaF_2 (2077, 1989, 1092, 1041, 963, 634, 608, 571 cm^{-1}) and on Si (2076, 2002, 1093, 1041, 963, 634, 603, 571 cm^{-1}). The band for the OH group (3570 cm^{-1}) confirms the data obtained by ultra-soft X-ray emission spectroscopy and Rutherford backscattering. The correspondence to nanocrystalline HAP was evaluated by an expert system as 99.03% on Si and as 99.32% on CaF_2.

Table 3. Element distribution across the thickness of a HAP coating on silicon.[37]

Depth /nm	Element concentration (at.%)			
	Ca	P	O	H
149.1	23.00 ± 1.15	11.00 ± 0.55	52.00 ± 2.60	14.00 ± 0.70
258.4	24.00 ± 1.20	12.00 ± 0.60	57.00 ± 2.85	7.00 ± 0.50
395.6	24.00 ± 1.20	14.00 ± 0.70	58.00 ± 2.90	4.00 ± 0.80
2233.4	24.00 ± 1.20	14.00 ± 0.70	60.00 ± 3.00	2.00 ± 0.40

The AFM scans of an electrochemically polished titanium foil surface, areas of different size of the surface of 1.0 μm-thick HA coating and roughness height distributions for the surface regions are shown in Fig. 15.[69] For relatively homogeneous relief, the surface height distribution in a 10.5×10.5 μm^2 area is in the range of 50 – 150 nm, which almost coincides with the distribution for the titanium substrate surface, being shifted to smaller heights when the survey area decreases to 3.5×3.5 μm^2. The two-level character of the coating growth front relief is clearly defined. The second-level relief is correlated with the HAP nanograin size revealed by TEM. Analysis of the surface morphology of the cross-section chip (see Fig. 9 *b*) showed that HAP growth is not accompanied by significant changes in the grain structure inherent in the growth of metallic coatings. This attests to low mobility of HAP components, which is insufficient for recrystallization during the growth typical of other materials.[121]

The annealing of thin (0.1 μm) free nanocrystalline HAP samples on a subject grid for 25 min at 650 °C in vacuum and in air induced recrystallization.[69] The grain size increased to 50 and 200 nm, respectively, the continuity being retained. The annealing for 1 h at 700 °C in air of amorphous films with minor inclusions of nanocrystalline HAP resulted in complete crystallization (Fig. 16 *a*). As a result, a single-phase structure (HAP) formed; a fragment of the electron diffraction pattern of this structure contains a full set of diffraction rings corresponding to the crystal lattice of HAP (Fig. 16 *b*).

The surface morphology of the HAP coatings formed in ion sputtering is quite suitable for using nanoindentation to certify their hardness. The general trend of nanoindentation and the dependence of the hardness on the coating structure are illustrated by Fig. 17.[22] The deformation of all samples is of elastoplastic type. The average hardness of amorphous structures is ~4.5 GPa, that of nanocrystalline structures is

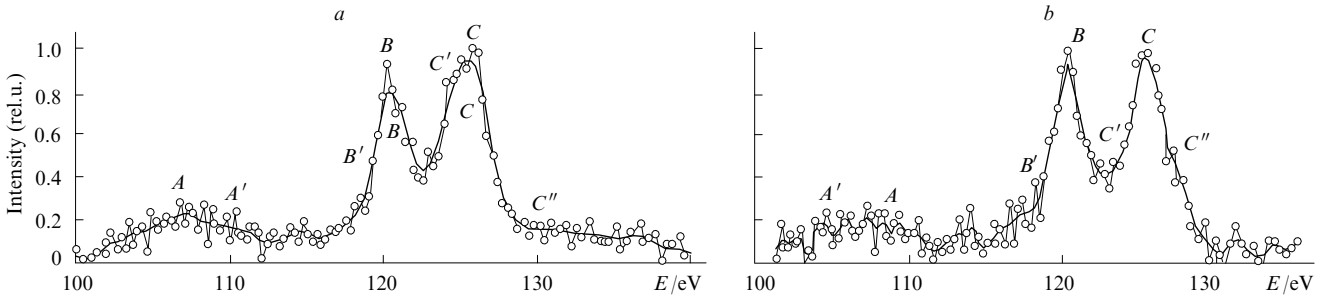


Figure 13. $L_{2,3}$ X-ray emission spectra of phosphorus for 0.1 μm-thick HAP coating on titanium (*a*) and microcrystalline HAP powder with a nearly stoichiometric composition (*b*).[37]

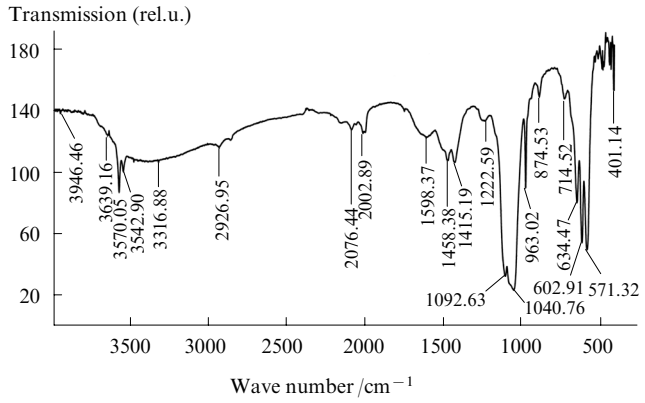


Figure 14. IR spectra of the 1.0 μm-thick HAP coating on the (111)Si surface.

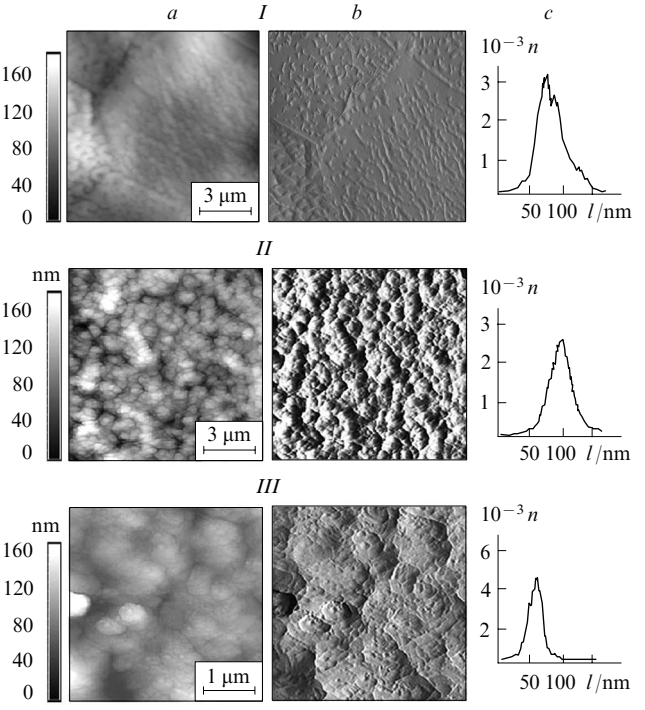


Figure 15. AFM scans of the surface in the topographic (*a*) and phase contrast (*b*) modes and surface height distribution (*c*).[69]
I is titanium foil; *II*, *III* are 1.0 μm-thick HAP coatings upon scanning of 10.5×10.5 and 3.5×3.5 μm^2 areas, respectively; (*l*) surface height, *n* is the number of irregularities (bulges).

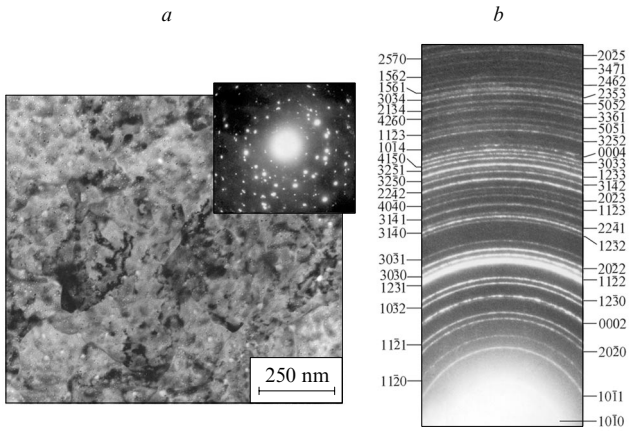


Figure 16. TEM image and microdiffraction pattern (*a*) and fragment of the electron diffraction pattern (*b*) of an HAP film formed after annealing in air.

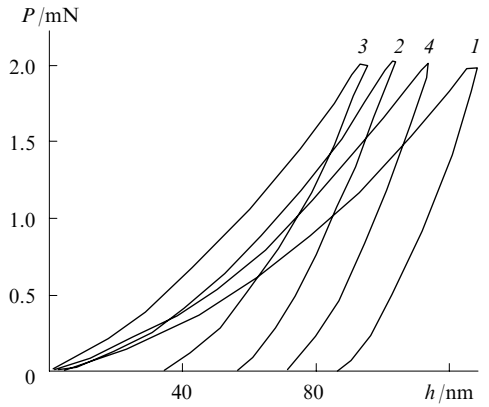


Figure 17. Hardness diagrams of 1.0 μm-thick HAP coatings on titanium.[22]
HAP ceramic coatings: (*1*) amorphous; (*2*, *3*) nanocrystalline before and after heat treatment, respectively; (*4*) nanocrystalline.

10.0 GPa before heat treatment and up to 11.5 GPa after annealing at 650 °C for 1 h; and the average hardness of dense ceramics with an average grain size of 60 nm is 7.0 GPa. These values are correlated with the data of another publication,[117] describing the hardness of coatings deposited by high-frequency magnetron sputtering and are much greater than the results of microindentation and nanoindentation of HAP ceramics: for example, 2.40 and 4.75 GPa for the piece parts synthesized by sintering in air and pressed at 180 and 250 MPa, respectively;[122] 6 ± 1 GPa for the submicrocrystalline HAP ceramics;[123] and 4.7 to 5.5 GPa upon the change of the ceramic structure from submicrocrystalline to nanocrystalline.[124] They approach the results of nanoindentation of composite ceramics, for example, HAP – boron nitride nanotubes (12 ± 2 GPa),[123] HAP – mullite (~ 9 GPa).[125]

The results of nanoindentation of compact nanocrystalline HAP coatings prepared by high-frequency magnetron sputtering approach the average values established for HAP microcrystals: 14.8 ± 0.1 GPa for the basis face and 9.5 ± 1.5 for the prismatic face.[21] A comparison of the data on the hardness of coatings and metallic materials showed considerable difference: unlike HAP, metallic single crystals are most plastic, the greatest hardness was achieved for nanocrystalline structures, and the intermediate values were found for amorphous structures; it is believed that the amorphous phase restricts the strength of nanocrystalline metallic structures.[126] The different type of the dependence of HAP hardness on the structure can be attributed to the non-dislocation mechanism of deformation with account of HAP atomic structure details. In metallic nanostructures, the intragrain deformation by the dislocation mechanism is limited by the grain size effect, and the grain-boundary sliding effect is switched on.[127]

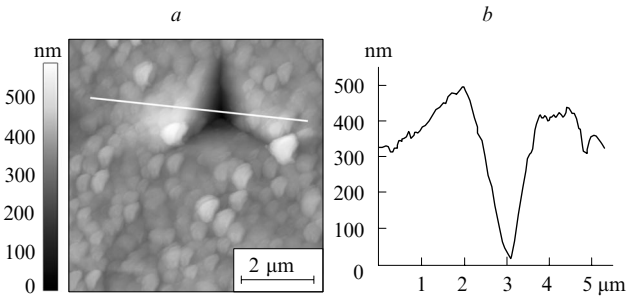


Figure 18. AFM image of the nanoindenter (*a*) and profile diagram along the distinguished line (*b*).

If the cluster $Ca_9(PO_4)_6$ is regarded as the structural unit of HAP, then the plasticity found for both amorphous calcium phosphate and crystalline HAP is attributable to mutual sliding of the clusters at lower intercluster (ionic) bonding as compared with stronger intracluster interatomic bonds (the covalent bond in the PO_4^{3-} group and ionic bonds with calcium atoms). Only the difference between the bonds at cluster boundaries in the crystalline HAP and in the amorphous calcium phosphate can account for the quantitative difference in their hardness. In nanocrystalline HAP at high loads, the grain boundary sliding may also play a role. The AFM image of the indentation for $P_{max} = 35$ mN and profile diagram along the line marked in the image are presented in Fig. 18. It can be seen that upward displacement of nanograin blocks is not almost accompanied by the change in their size. A nanofracture starts to appear at this load.

The scratch test charts illustrating the change in the parameters that determine the damage threshold and adhesive strength are shown in Fig. 19.[37] Since the hardness of the HAP coating is higher than that of the titanium substrate, the moment of coating abrasion was accompanied by fast immersion of the indenter into the sample, sharp increase in the friction coefficient, an acoustic emission burst and amplitude increase (the lower the material hardness, the greater the noise caused by acoustic emission). Testing of HAP coatings with thickness of 1.0 μm on nonmodified titanium surface showed low adhesive strengths (up to 2.5 N) (see Fig. 19 *a*). The low adhesive strength can be attributed to the formation of a thin layer of brittle titanium suboxide Ti_6O at the interface.

Upon deposition on titanium of an intermediate film by magnetron sputtering of titanium in air environment, the adhesive strength increased: for a coating formed above the erosion zone of the target, it reached 7.0 N (see Fig. 19 *b*); for a coating formed beyond this position, it was up to 4.0 N (see Fig. 19 *c*). The maximum adhesive strength (12.8 N) was achieved on titanium substrates modified by the composite intermediate layer $TiC + TaC + Ca_3(PO_4)$ (see Fig. 19 *d*). The character of exfoliation and the character of signals indicate that at a critical load, the HAP coating detaches from the substrate together with the intermediate layer, which attests to higher adhesive strength of the HAP/intermediate layer interface and the cohesive strength of

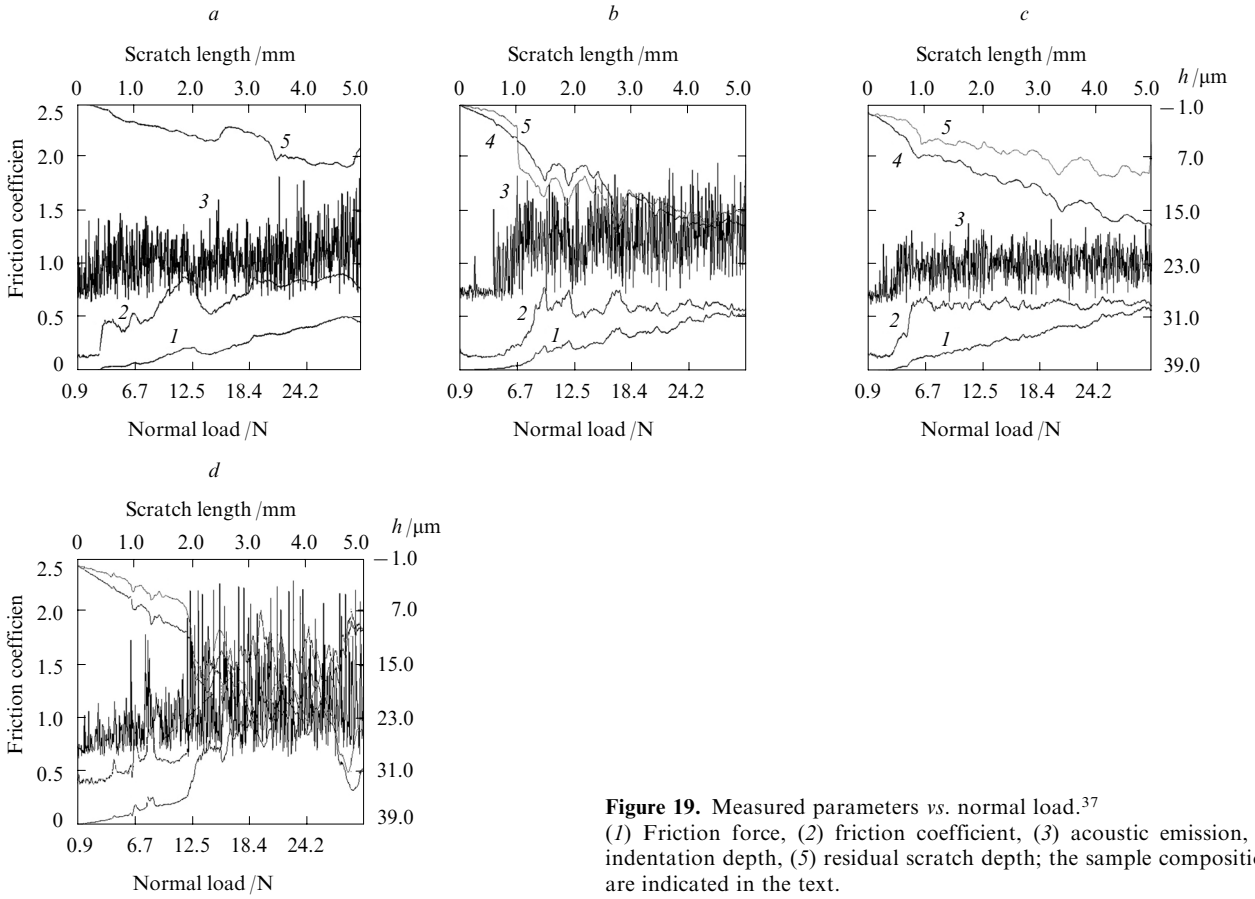


Figure 19. Measured parameters *vs.* normal load.[37]
(*1*) Friction force, (*2*) friction coefficient, (*3*) acoustic emission, (*4*) indentation depth, (*5*) residual scratch depth; the sample compositions are indicated in the text.

HAP compared with the adhesive strength of the intermediate layer/titanium interface. The composite intermediate layer was chosen relying on high mechanical characteristics of these coatings found by the authors.[49] A way of controlling the coating structure and increasing the adhesion is the subsequent photon treatment. The first studies of fast photon annealing by IR radiation demonstrated [128] the possibility to control the solubility of the coatings. After pulsed photon treatment by radiation from high-power xenon lamps, the adhesion of the coatings increased 2.5 – 3-fold as a result of activation of solid-phase reactions at the interface.[69]

As noted above, the ion beam sputtering produces amorphous structures unsuitable for application due to high dissolution rate. Enhancement of the adhesion and the possibility of controlling the structure (an, hence, the solubility) of the coatings can be achieved by using so-called ion beam assisted deposition (IBAD) technique.[129, 130] In particular, Choi *et al.*[131] applied this method to the formation of a HAP coating with gradient crystallinity. In early stages, the assisting beam ensured mixing of atoms deposited from the flux with the substrate atoms (this increased the adhesive strength), and at subsequent stages it activated crystallization. When the Ca : P ratio in the target was close to 1.6, the coating was formed with ratio Ca : P $\approx$ 1.46.

The ion assistance was less efficient in the case of electron-beam evaporation of HAP and condensation:[130, 131] the coatings remained amorphous. In the electron-beam evaporation, the Ca : P ratio increased, while the ion assistance to the condensation led to its decrease. Generally, despite the increase in the adhesive strength to 64.8 MPa [132] (much greater than in the plasma spray process), this version of IBAD cannot be recognized as commercially promising.

A comparison of the structure and morphology of the surfaces of coatings formed upon high-frequency magnetron sputtering and in the plasma spray process revealed the following advantages of the former method:

— the morphological and structural uniformity allows prediction of the coating behaviour in the body,

— small thickness leads to higher fracture toughness,

— nanocrystalline structure increases the biological activity.

Therefore, the view about good prospects of high-frequency magnetron sputtering for the deposition of CP coatings stated in the review [14] appears substantiated.

IV. Conclusion

Despite the diversity of approaches to the synthesis of biologically active coatings on metallic implants, the main practically used method is plasma spray deposition due to its high productivity. However, with clearly pronounced morphological, phase and structural heterogeneity of these coatings, they remain least studied.

The views on the microscopic levels of the structure of metal/ceramics interfaces, grain boundaries and phase interfaces in the ceramic coating have not been developed. No systematic elaboration of approaches to increasing the adhesive strength, controlling the morphological organization of CP coatings formed by physical methods and to creating gradient structures ensuring the specified kinetics of resorption were carried out.

Despite the sufficient accumulation of data on the regularities of deformation of CP coatings, the views on the microscopic mechanism of plasticity observed in the indentation of HAP coatings with different structures have not been developed. No biologically substantiated recommendations on the thickness of CP coatings taking account of their real structure for each synthetic method were proposed.

This work was performed with the financial support of the Russian Foundation for Basic Research (Project No. 11-03-90426-ukr_f_a) and the Ministry of Education and Science of the RF (Federal Target Programme 'Scientific and Scientific – Pedagogical Personnel of the Innovative Russia in 2009 – 2013', agreement No. 8299).

References

1. M Epple *Biomaterialien und Biomineralisation* (Wiesbaden: Teubner Verlag, 2003)
2. J Ellinggen *Biomaterials* **12** 593 (1991)
3. R Z Valiev, I P Semenova, V V Latysh, A V Shcherbakov, E B Yakushina *Nanotekhnol. Russ.* **3** 593 (2008)
4. D Schruweber, R Beutner, S Rosler, H Worch *J. Mater. Sci.: Mater. Med.* **13** 1215 (2002)
5. Yu R Kolobov *Nanotekhnol. Russ.* **4** 758 (2009)
6. M Jayaraman, U Meyer, M Buchner, U Joos, H-P Wiesman *Biomaterials* **25** 625 (2004)
7. H A Shalaby, A M Naschem, N A Bodr, M M Shoeib, M G Khofagy *J. Am. Sci.* **7** 574 (2011)
8. L Jacominc, These Doctor de I Université de Strasbourg, Strasbourg, 2010
9. S M Barinov *Russ. Chem. Rev.* **79** 13 (2010)
10. T Kanazava *Neorganicheskie Fosfatnye Materialy* (Inorganic Phosphate Materials) (Eds A P Shpak, V L Karbovskii) (Kiev: Naukova Dumka, 1998)
11. A P Shpak, V L Karbovskii, V V Trachevskii *Apatity* (Apatites) (Kiev: Akademperiodika, 2002)
12. S M Barinov, V S Komlev *Biokeramika na Osnove Fosfatov Kal'tsiya* (Bioceramics Based on Calcium Phosphates) (Moscow: Nauka, 2005)
13. S M Barinov, V S Komlev *Calcium Phosphate Based Bioceramics for Bone Tissue Engineering* (Zürich: Trans Tech Publ., 2008)
14. R Narayaman, S K Seshadri, T Y Kwon, K N Kim *J. Biomed. Mater. Res. B* **85** 279 (2008)
15. W Xia, C Lindahl, J Lausmaa, H Engvist, in *Advances in Biomimetics* Ch. 20 (Ed. A George) (Vienna: InTech, 2011) p. 429
16. V I Kalita *Fiz. Khim. Obrab. Mater.* (5) 28 (2000)
17. E van der Wal, Thesis Doctor, Universiteit Utrect, Utrect, 2003
18. A Carradò, H Pelletier, T Roland, in *Biomedical Engineering — from Theory to Applications* Ch. 11 (Ed. R Fazel-Rezai) (Vienna: InTech, 2011) p. 253
19. A G Veresov, Candidate Thesis in Chemical Sciences, Moscow State University, Moscow, 2003
20. J P Hirt, J Lothe *Theory of Dislocations* (Vew York: McGraw-Hill, 1968)
21. B Viswanath, R Raghavan, V Ramamarty, N Ravishankar *Scr. Mater.* **57** 361 (2007)
22. V M Ievlev, S M Barinov, A V Kostyuchenko, E K Belonogov *Materialovedenie* (6) 22 (2010) [a]
23. W Bollmann *Crystal Defects and Crystalline Interfaces* (Berlin, Heidelberg, New York: Springer, 1970)
24. A Petak, J Reid, M Stott, M Sauer *Biomaterials* **28** 4023 (2007)
25. I Suvorova, P A Buffat *J. Microsc.* **196** 46 (1999)

26. A S Fomin, N V Plokhikh, I V Fadeeva, S M Barinov, V M Ievlev, S A Soldatenko *Dokl. Chem.* **435** 347 (2010)
27. M A Gol'dberg, V V Smirnov, V M Ievlev, S M Barinov, S B Kutsev, T V Shibaeva, L I Shvorneva *Inorg. Mater.* **48** 181 (2012)
28. S M Barinov, V M Ievlev, V S Komlev, S B Kushchev, Yu A Ponomarev, A A Sinel'nikov, S A Soldatenko *Konden. Sredy Mezhfaz. Granitsy* **12** 22 (2010)
29. T Aoba, J Takanashi, T Yagi, M Okazaki, Y Moriwaki *J. Dent. Res.* **57** 708 (1978)
30. A M Porter, S M Best, W Bonfield *J. Biomed. Mater. Res. A* **68** 133 (2004)
31. K Sato, T Kogure, H Iwai, J Tanaka *J. Am. Ceram. Soc.* **85** 3054 (2002)
32. V M Ievlev, S M Barinov, A V Kostyuchenko, A S Prizhimova, V V Smirnov *Dokl. Chem.* **437** 57 (2011)
33. P H Pumphrey *Scr. Metall.* **7** 893 (1973)
34. P H Pumphrey *Phys. Status Solidi A* **28** 545 (1975)
35. V M Ievlev, K A Solntsev, A A Sinel'nikov, S ASoldatenko *Inorg. Mater.: Appl. Res.* **2** 70 (2011)
36. V M Kosevich, V M Ievlev, L S Palatnik, A I Fedorenko *Struktura Mezhkristallitnykh Mezhfaznykh Granits* (Structure of Intergranular and Interphase Boundaries) (Moscow: Metallurgiya, 1980)
37. V M Ievlev, E P Domashevskaya, V I Putlaev, Yu D Tretyakov, S M Barinov, A V Kostyuchenko, M I Petrzhik *Glass Phys. Chem.* **34** 608 (2008)
38. M Tamai, T Isshiki, K Nishio, M Nakamura, A Nakahira, H Endon *J. Mater. Sci.* **41** 525 (2006)
39. W E Brown *Nature (London)* **196** 1048 (1962)
40. M E Fernandez, C Zorilla-Cangus, R Carcia-Carcia, J A Assencio, J Reyes-Gasga *Acta Crystallogr., Sect. B* **59** 175 (2003)
41. E I Suvorova, P A Buffat *Eur. Cells Mater.* **1** 27 (2001)
42. S Nath, K Biswas, B Basu *Scr. Biomater.* **58** 1054 (2008)
43. G Doculsi, B Kerebel *J. Biol. Buccule* **5** 203 (1977)
44. D Ferro, S M Barinov, J V Ran, R Feghil, A Latini *Biomaterials* **26** 805 (2005)
45. K Ozeki, H Aoki, T Masuzawa *J. Austr. Ceram. Soc.* **46** 59 (2010)
46. K A Gross, V Gross, C C Berndt *J. Am. Ceram. Soc.* **81** 106 (1998)
47. I V Shishkovsky, E Yu Tarasova, L V Zhuravel', A L Petrov *Tech. Phys. Lett.* **27** 211 (2001)
48. B-Y Chou, E Chang *Scr. Mater.* **45** 487 (2001)
49. D V Shtanskyi, M I Petrzhik, I A Bashkova, F V Kiryukhantsev-Korneev, A N Sheveiko, E A Levashov *Phys. Solid State* **48** 1301 (2006)
50. V Nelea, C Morosanu, M Iliescu, I N Mihailescu *Surf. Coat. Technol.* **173** 315 (2003)
51. V Putlayev, A Veresov, M Pulkin, A Soin, V Kuznetsov *Mat.-Wiss. Werkstoff. Technol.* **37** 416 (2006)
52. X Yin, L Calderin, M J Stott, M Sauer *Biomaterials* **23** 4155 (2002)
53. P V Evdokimov, A V Soin, A G Veresov *Al'ternativ. Energ. Ecol.* **1** 77 (2007) [b]
54. M A Surmeneva, M V Chaikina, R A Surmenev, A A Kachaev, V F Pichugin, M Epple *Fiz. Khim. Obrab. Mater.* (3) 51 (2012)
55. K Onuma, A Ito, T Tateishi *J. Cryst. Growth* **167** 773 (1996)
56. N Kanazaki, K Onuma, A Ito, K Teraoka, T Tateishi, S Tsutsumi *J. Phys. Chem.* **102** 6471 (1998)
57. I V Melikhov, V F Komarov, A V Severin, V E Bozhevol'nov, V N Rudin *Dokl. Phys. Chem.* **373** 125 (2000)
58. K Onuma, A Ito *Chem. Mater.* **10** 3346 (1998)
59. B Posner *Acc. Chem. Res.* **8** 277 (1975)
60. N C Blumental, A S Posner, J M Holmes *Mater. Res. Bull.* **7** 1181 (1972)
61. R A Harper, A S Posner *Mater. Res. Bull.* **5** 129 (1970)
62. S N Danil'chenko *Visnik SumDU. Fiz. Mat. Mekhan.* **2** 33 (2007)
63. A Ito *Biomaterials* **22** 2921 (2001)
64. Yu Ya Tomashpol'skii, G A Platonov *Segnetoelektricheskie Plenki Slozhnykh Okislov Metallov* (Ferroelectric Films of Complex Metal Oxides) (Moscow: Metallurgiya, 1978)
65. P Serra, J L Morenza *Appl. Surf. Sci. Proc.* **67** 289 (1998)
66. B Feng, J Weng, B C Yang, S X Qu, X D Zhang *Biomaterials* **24** 4663 (2003)
67. M Uchida, H M Kim, T Kokubo, S Fypbayashi, T Nakamura *J. Biomed. Mater. Res. A* **64** 164 (2003)
68. S R Sousa, M A Barbosa *Biomaterials* **17** 397 (1996)
69. A V Kostyuchenko, Candidate Thesis in Physical and Mathematical Sciences, Voronezh State Technical University, Voronezh, 2009
70. X Zheng, M Huang, C Ding *Biomaterials* **21** 841 (2000)
71. F Liang, L Zhou, K Wang *Surf. Coat. Technol.* **165** 133 (2003)
72. X Zhu, D W Son, J L Ong, K H Kim *J. Mater. Sci. Mater. Med.* **14** 629 (2003)
73. Y Han, T Fu, J Lu, K Xu *J. Biomed. Mater. Res. A* **54** 96 (2001)
74. T Kokubo, H Kushitani, S Sakka, T Kitsugi, T Yamamuro *J. Biomed. Mater. Res. A* **24** 721 (1990)
75. A Bigi, E Boanini, B Bracci, A Facchini, S Panzavolta, F Segatti, L Struba *Biomaterials* **26** 4085 (2005)
76. B Feng, Y Chen, X D Zhang *J. Biomed. Mater. Res. A* **59** 12 (2002)
77. H B Wen, J G C Wolke, J R de Wijn, Q Liu, F Z Cui *Biomaterials* **18** 1471 (1997)
78. M T Pham, W Matz, H Reuther, E Richter, G Steiner, S Oswald *Surf. Coat. Technol.* **128 – 129** 313 (2000)
79. W Wu, G Nancollas *J. Colloid. Inter. Sci.* **199** 206 (1998)
80. G Nancollas, W Wu, R Tang *Glass Sci. Technol.-Glastech. Ber.* **73** 318 (2000)
81. C Mao, H Li, F Cui, C Ma, Q Feng *J. Cryst. Growth* **206** 308 (1999)
82. C Lindahl, P Borchardt, J Lausmaa, W Xia, H Engqvist *J. Mater. Sci. Med.* **21** 2743 (2010)
83. V M Ievlev, K A Solntsev, S A Soldatenko, L Yu Leonova, P V Novikov, E V Golosov, A A Sinel'nikov, A M Vozgor'kov *Inorg. Mater.: Appl. Res.* **3** 282 (2012)
84. R Narayanan, S K Seshadri, T-Y Kwon, K-H Kim *Scr. Mater.* **56** 229 (2007)
85. X Meng, T-Y Kwon, K-H Kim *Key Eng. Mater.* **309 – 311** 639 (2006)
86. B Surovsca, J Bienas *J. Achiev. Mater. Manufact. Eng.* **43** 162 (2010)
87. D M Liu, T Troczynski, W J Tseng *Biomaterials* **22** 1721 (2001)
88. M H Fatti, A Hanifi *Mater. Lett.* **61** 3978 (2007)
89. H-W Kim, H-E Kim, J C Knowles *Biomaterials* **25** 3351 (2004)
90. A Balamurugan, S Kannan, S Rajeswari *Trends Biomater. Artif. Organ.* **16** 18 (2002)
91. S Zhang, Y S Wang, X T Zeng, K Cheng, M Qian, D E Sun, W I Weng, W Y Chia *Eng. Fract. Mechan.* **74** 1884 (2007)
92. D M Liu, Q Yang T Troczynski, W J Tseng *Biomaterials* **23** 1679 (2002)
93. U Vijayalakshmi, S Rajeswari *Trends Biomater. Artif. Organ.* **19** 57 (2006)
94. C Battistoni, M P Casaletto, G M Ingo, S Kociulis, G Mattagno, L Pandolsi *Surf. Interface Anal.* **29** 773 (2000)
95. K A Gross, C C Berndt *J. Biomed. Mater. Res. A* **39** 580 (1998)
96. K A Gross, C C Berndt, H A Herman *J. Biomed. Mater. Res. A* **39** 407 (1998)
97. K A Gross, M Babolic *Biomaterials* **23** 4731 (2002)

98. M Vilotijevic, P Markovic, S Zec, S Marinkovic, V Jokanovic *J. Mater. Proc. Technol.* **211** 996 (2011)
99. V F Bochkarev, S M Barinov, V V Naumov *Perspekt. Mater.* **6** 55 (2003)
100. W D Tong, J Y Chen, X D Li, J M Feng, Y Cao, Z J Yang X D Zhang *J. Mater. Sci.* **31** 3739 (1996)
101. A van der Drift *Phil. Res. Rep.* **22** 267 (1967)
102. H H Pan, J H Tao, X W Yu, L Fu, J L Zhang, X X Zeng, G Xu, R K J Tang *Phys. Chem. B* **112** 7162 (2008)
103. A Carrado *J. Coat. Technol. Res.* **8** 749 (2011)
104. A Dey, A K Mukhopadhyay, S Gangadharan, M K Sinha, D Basu *J. Mater. Sci.* **44** 4911 (2009)
105. Yu I Golovin *Nanoindentirovanie i ego Vozmozhnosti* (Nanoindentation and Its Ability) (Moscow: Mashinostroenie, 2009)
106. V M Ievlev, S M Barinov, V I Kalita, A V Kostyuchenko, A T Pugachev, in *Materialy VI Vserossiiskoi Konferentsii 'Fiziko-khimicheskie Protsessy v Kondensirovannykh Sredakh i na Mezhfaznykh Granitsakh'* (Proceedings of the VIth Conference 'Physicochemical Processes in Condensed Media and on Interfaces') (Voronezh: Nauchnaya Kniga, 2012) p. 190
107. W S Oliver, G M Pharr *J. Mater. Res.* **19** 3 (2004)
108. W Weibull *Proc. Roy. Swedish Inst. Eng. Res. Rep.* **151** 121 (1939)
109. A Dudek *Opt. Appl.* **39** 825 (2009)
110. C F Koch, S Johnson, D Kumar, M Jelinek, D B Chrisey, A Draiswamy, C Jin, R J Narayan, N M Mihailescu *Mater. Sci. Eng. C* **27** 484 (2007)
111. S S Alimpiev, E E Antonov, V N Bagratashvili, A A Doktorov, I O Kovalev, V B Likhanov, S M Nikiforov, V K Popov, E N Sobol' *Stomatologiya* (5) 64 (1996)
112. W J Lee, S W Lee, H L Kim, D J Kim *J. Korean Phys. Soc.* **47** 152 (2005)
113. V Nelea, H Pelletier, M Iliescu, J Werskmaun, V Craciun, I N Minailescu, C Ristoscu, C Ghice *J. Mater. Sci.-Mater. Med.* **13** 167 (2002)
114. S Grigorescu, C Ritoscu, C Socol, E Axente, F Feugeas, I N Michailescu *Rom. Rep. Phys.* **57** 1003 (2005)
115. V Ievlev, A Kostychenko, M Sumets, V Vakhtel *J. Mater. Sci.: Mater. Electron.* **22** 1258 (2011)
116. J G C Wolke, K De Groot, J A Jansen *J. Mater. Sci.* **33** 3371 (1998)
117. K van Dijk, H G Shaeken, J G Wolke, K de Groot, J A Jansen *J. Biomed. Mater. Res. A* **29** 269 (1995)
118. V F Pichugin, S I Tverdokhlebov, R A Surmenev, E V Shesterikov, M A Ryabtseva, A A Kozel'skaya, I A Shulepov *Russ. Phys. J.* **49** 320 (2006)
119. Z Hong, L Luan, S Paik, B Deng, D Ellis, J Keterson, A Mello, J Eon, Y Terra, A Rossi *Thin Solid Films* **515** 6773 (2007)
120. S M Barinov, E K Belonogov, V M Ievlev, A V Kostyuchenko, V I Putlyaev, Yu D Tretyakov, V V Smirnov, I V Fadeeva *Dokl. Phys. Chem.* **412** 15 (2007)
121. V M Ievlev *Tonkie Plenki Neorganicheskikh Materialov: Mekhanizm Rosta i Struktura* (Thin Films of Inorganic Materials: Growth Mechanism and Structure (Voronezh: Voronezh State University, 2008)
122. M Monteiro, W M Lima, M V Oliveira, A M Rossi, in *The 6th Latin American Congress of Artificial Organs and Biomaterials, Gramados-Brasil, 2010*
123. D Lahiri, V Singh, A P Benaduce, S Seal, L Kos, A Agarwal *J. Mechan. Behav. Biomed. Mater.* **4** 44 (2011)
124. J Wang, L L Shaw *J. Am. Ceram. Soc.* **93** 601 (2010)
125. S Nath, A Dey, A K Mukhopadhyay, B Basu *Mater. Sci. Eng. A* **513** – **514** 197 (2009)
126. O K Belousov, N A Palii, V T Zabolotnyi *Russ. Metall.* (1) 33 (2011)
127. R A Andrievskii, A M Glezer *Pysics-Uspekhi* **52** 315 (2009)
128. M Yoshinari, T Hayakava, J G C Wolke, K Nemoto, J A Jansen *J. Biomed. Mater. Res.* **37** 60 (1997)
129. F Z Cui, Z S Luo, Q L Feng *Mater. Sci.: Mater. Med.* **8** 403 (1997)
130. A Rabiei, B Thomas *Mater. Res. Soc. Symp. Proc.* **845** 193 (2005)
131. J-M Choi, H-E Kim, J-S Lee *Biomaterials* **21** 469 (2000)
132. J-S Lee, C-N Whang, H-E Kim, J-C Park, J H Song, S-R Kim *Mater. Sci. Eng. C* **22** 15 (2002)

[a] — *Inorg. Mater.: Appl. Res. (Engl. Transl.)*
[b] — *Int. Sci. J. Alter. Energ. Ecol. (Engl. Transl.)*